JOURNAL OF PETROLOGY

Journal of Petrology, 2017, Vol. 58, No. 1, 3–28
doi: 10.1093/petrology/egw070
Advance Access Publication Date: 10 January 2017
Original Article

OXFORD

Nb/Ta Fractionation by Amphibole in Hydrous Basaltic Systems: Implications for Arc Magma Evolution and Continental Crust Formation

L. Li[1,2], X. L. Xiong[1]* and X. C. Liu[1]

[1]State Key Laboratory of Isotope Geochemistry, Chinese Academy of Sciences, Guangzhou 510640, China, [2]University of the Chinese Academy of Sciences, Beijing 100049, China

*Corresponding author. Telephone: +0086 20 85290287. Fax: 0086 20 85290287. E-mail: xiongxl@gig.ac.cn

Received October 18, 2015; Accepted November 23, 2016

ABSTRACT

To understand fully the role of amphibole in the fractionation of Nb/Ta during arc magma evolution, we conducted experiments with mid-K and high-K basalts to determine amphibole/melt Nb, Ta and Ti partition coefficients (D_{Nb}, D_{Ta} and D_{Ti}) at variable conditions of bulk TiO_2, P, T, H_2O and fO_2. The experimental results show that, at crustal pressures, amphibole is the most important crystalline phase in hydrous basaltic systems. The amphibole/melt Nb, Ta, and Ti partitioning results are 0·16–0·90 for D_{Nb}, 0·13–0·68 for D_{Ta}, 1·81–10·63 for D_{Ti} and 0·76–2·81 for D_{Nb}/D_{Ta}. Bulk TiO_2 and fO_2 show no observable effects. T and H_2O, in addition to the compositions of amphibole and melt, are the main affecting factors. D_{Nb}, D_{Ta}, D_{Ti} and D_{Nb}/D_{Ta} increase with decreasing temperature, amphibole Mg# and melt H_2O content and increasing melt polymerization. During cooling and crystallization of arc magmas at crustal pressures, amphibole Mg# decreases and melt polymerization increases, leading to significant increase in amphibole/melt D_{Nb}, D_{Ti} and D_{Nb}/D_{Ta}. Nb/Ta fractionation in evolved melts will thus be enhanced with crystallization progress. Meanwhile, melt H_2O content will increase with the degree of crystallization, which slows down the increase in these D values. Therefore, the trend and extent of Nb/Ta fractionation in the melt by amphibole critically depends on temperature and melt H_2O content. Only low temperatures or low H_2O contents at high temperatures lead to high D values. For arc magmas with an average H_2O of ~3·9 wt %, D_{Nb} and D_{Nb}/D_{Ta} are in general >0·40 and >1·20, respectively, which explains why amphibole fractionation results in lower Nb/Ta ratios in evolved arc magmas. The bulk Nb/Ta fractionation trend during arc magma evolution appears to be generally controlled by fractional crystallization of amphibole. Experimental and modeling results suggest that amphibole is a main fractionating phase during arc magma evolution and continental crust formation.

Key words: amphibole, Nb and Ta partition coefficients, arc magmas, Nb/Ta fractionation

INTRODUCTION

The geochemistry of Nb and Ta is very important in understanding Earth's core–mantle differentiation and continental crust formation. The Nb/Ta ratios of the accessible silicate reservoirs (Fig. 1) are lower than the chondritic value of 17·5 (Jochum *et al.*, 2000) or 19·9 (Munker *et al.*, 2003). The assumption of a chondritic Nb/Ta for the Earth means that core–mantle differentiation has led to sub-chondritic Nb/Ta ratios in the silicate Earth (Munker *et al.*, 2003; Cartier *et al.*, 2014), or that crust–mantle differentiation has produced super-chondritic Nb/Ta reservoirs hidden in the deep mantle (Rudnick *et al.*, 2000; Tiepolo & Vannucci, 2014). Furthermore, the present-day andesitic bulk continental crust has Nb/Ta of 12–13 (Barth *et al.*, 2000), generally lower than in terrestrial basalts. The Nb/Ta ratios in Archean tonalite–trondhjemite–granite (TTG) terranes are also highly variable relative to those of basalts.

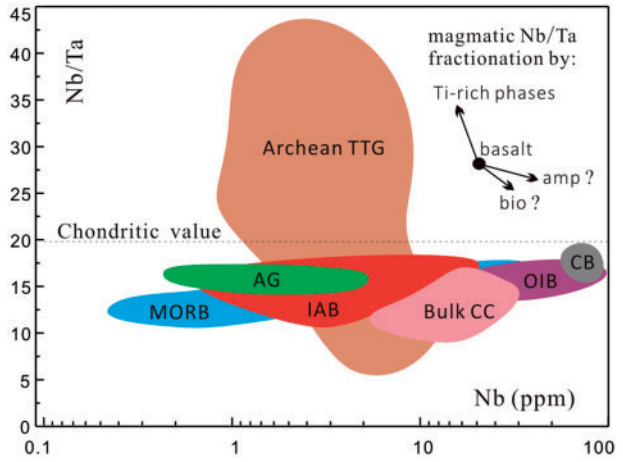

Fig. 1. Contrasting Nb/Ta ratios between terrestrial basalts (MORB, OIB, CB and IAB) and continental crustal rocks (bulk CC and Archean TTG), showing that Nb/Ta in Archean TTG is highly variable, but it is generally lower in the bulk CC than in terrestrial basalts from different geological settings. MORB, mid-ocean ridge basalts; OIB, ocean island basalts; CB, continental basalts; IAB, island arc basalts; AG, Archean greenstones; TTG, tonalite–trondhjemite–granite; CC, continental crust; amp, amphibole; bio, biotite. Data sources: MORB, OIB, CB, IAB and AG from Munker *et al.* (2003, 2004); Archean TTG from Hoffmann *et al.* (2011); bulk CC from Barth *et al.* (2000). Possible Nb/Ta fractionation trends caused by key minerals are also indicated.

Given that basalts are the precursors of intermediate–felsic magmas, these indicate significant Nb/Ta fractionation during continental crust formation. Generation of intermediate–felsic magmas is, in general, ascribed to partial melting of mafic rocks or fractional crystallization of mafic magmas (e.g. Rudnick & Gao, 2003; Hawkesworth & Kemp, 2006). During these processes, Nb/Ta fractionation by olivine, orthopyroxene, clinopyroxene, spinel or garnet is negligible, as these minerals have extremely low mineral/melt Nb (D_{Nb}) and Ta (D_{Ta}) partition coefficients (<0·01; Adam & Green, 2006). Although amphibole, biotite and Ti-rich phases (rutile, titanite and ilmenite) have higher D_{Nb} and D_{Ta} and variable D_{Nb}/D_{Ta}, they must be the main candidates for Nb/Ta fractionation during continental crust formation.

Rutile and other Ti-rich phases are the major carriers of Nb and Ta in crustal rocks (Zack *et al.*, 2002; Xiao *et al.*, 2006; Xiong *et al.*, 2009). D_{Nb}/D_{Ta} values for these phases are generally ≤1·0 (Xiong *et al.*, 2011, and references therein). They thus impart only elevated or unchanged Nb/Ta ratios to coexisting melts. Their fractional crystallization explains the higher or equal Nb/Ta ratios of most TTGs relative to their mafic precursors (Hoffmann *et al.*, 2011; John *et al.*, 2011; Xiong *et al.*, 2011), but cannot explain the lower Nb/Ta ratios in the bulk continental crust and the low Nb/Ta endmembers of the TTG. Amphibole (Tiepolo *et al.*, 2000) and biotite (Stepanov & Hermann, 2013) are the only two phases that have the ability to impart lower Nb/Ta to coexisting melts. However, biotite typically crystallizes from more evolved, K-enriched felsic magmas and generally cannot account for the low Nb/Ta ratios of the andesitic continental crust. Therefore, amphibole is potentially the main phase responsible for these low Nb/Ta ratios. Amphibole-dominated fractionation of arc magmas in the roots of the arc crust has been widely recognized as the fundamental process for producing intermediate–felsic magmas (e.g. Davidson *et al.*, 2007; Dessimoz *et al.*, 2012). Nb/Ta fractionation by amphibole is thus of key importance for understanding arc magma evolution.

Experiments (Supplementary Data Table S1-1; supplementary data are available for downloading at http://www.petrology.oxfordjournals.org) have been conducted to determine amphibole/melt Nb and Ta partitioning. Most previous studies focused on basanitic and alkali basaltic compositions (Adam *et al.*, 1993, 2007; Dalpé & Baker, 2000; Tiepolo *et al.*, 2000; Adam & Green, 2003) because large amphibole crystals grow easily from melts of such composition, whereas data for calc-alkaline arc magmas still remain rare. According to the literature (Fig. 2), amphibole/melt D_{Nb} and D_{Ta} are highly variable: 0·07–0·80 for D_{Nb}, 0·06–0·80 for D_{Ta} and 0·69–1·63 for D_{Nb}/D_{Ta}. These data indicate that amphibole may impart a lower, equal or even higher Nb/Ta ratio to the melt. The high variability of D_{Nb}/D_{Ta} (from <1·0 to >1·0) raises the questions: what are the main factors controlling amphibole–melt Nb and Ta partitioning and why does amphibole fractionation result in lower Nb/Ta ratios in evolved arc magmas? In addition, it is well known that the behavior of Nb and Ta is similar to that of Ti in magmatic processes, and that arc magmas and the average continental crust have pronounced negative anomalies in Nb, Ta and Ti. Thus, it is also necessary to evaluate whether or not there are any correlations between these anomalies and Nb/Ta fractionation during arc magma evolution.

In previous studies it was demonstrated that D_{Nb}, D_{Ta}, D_{Ti} and D_{Nb}/D_{Ta} increase with decreasing amphibole Mg# and increasing melt polymerization (Tiepolo *et al.*, 2007, 2000), and that D_{Nb}, D_{Ta} and D_{Ti} increase with decreasing pressure with no obvious change of D_{Nb}/D_{Ta} (Adam *et al.*, 2007). However, the effects of bulk composition, temperature and H_2O content are still unclear. For better understanding of the role of amphibole in the fractionation of Nb/Ta during arc magma evolution, we conducted systematic experiments with mid-K and high-K basalts to determine the amphibole/melt D_{Nb}, D_{Ta} and D_{Ti} at variable conditions of bulk TiO_2, P, T and H_2O. In combination with the published data, these data provide a more complete picture of amphibole/melt Nb, Ta and Ti partitioning and allow us to constrain the main factors controlling the Nb/Ta fractionation in hydrous arc basalt systems.

EXPERIMENTAL AND ANALYTICAL METHODS

Starting compositions and initial H_2O contents

Arc basalts can span a wide range of compositions from low to high K. Because low-K compositions are

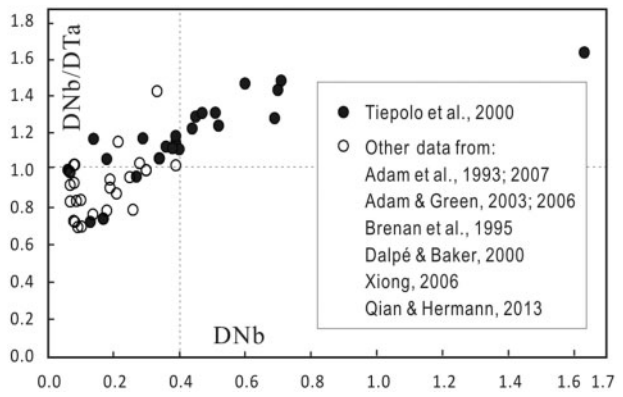

Fig. 2. Literature data (Adam & Green, 2003, 2006; Adam *et al.*, 1993, 2007; Brenan *et al.*, 1995; Dalpe & Baker, 2000; Qian & Hermann, 2013; Tiepolo *et al.*, 2000; Xiong *et al.*, 2006; Supplementary Data Table S1-1) for amphibole/melt D_{Nb} and D_{Ta}, showing that D_{Nb}/D_{Ta} values from Tiepolo *et al.* (2000) are mostly >1·0, whereas D_{Nb}/D_{Ta} values from other studies are generally ≤1·0. The data of Klein *et al.* (1997) and Hilyard *et al.* (2000) are not shown here, as their experimental charges were doped with 0·5% Nb and 0·5% Ta (much higher than in natural systems) and Henry's Law partitioning behavior was not demonstrated. In addition, the amphibole/melt Fe–Mg K_D values (0·01–0·18) of Hilyard *et al.* (2000) indicate disequilibrium crystallization.

experimentally difficult in producing large amphibole crystals, we chose mid-K (MKB) and high-K (XT168N) basalts (Table 1) for our experiments. The high-K basalt is a natural sample from Chinese Tianshan, whereas the mid-K basalts include four synthetic compositions MKB-0, MKB-0.3, MKB-0.6 and MKB-1.2 with TiO_2 varying from 0·0 to 0·3, 0·6 and 1·2 wt %; these were synthesized from reagent grade oxides SiO_2, TiO_2, Al_2O_3, Fe_2O_3 and MgO and carbonates $CaCO_3$, Na_2CO_3 and K_2CO_3 using two rounds of melting–quenching–grinding. The variation of TiO_2 content in this series helps to investigate the effect of Ti in amphibole on the Nb and Ta partitioning. All five compositions were respectively doped with ~100 ppm of Nb_2O_5 and Ta_2O_5 to ensure Henry's Law partitioning behavior and analytical precision with laser ablation inductively coupled plasma mass spectrometry (LA-ICP-MS, especially at the small spot condition (Table 2)); ~100 ppm of CsCl was also added to each of the starting materials to facilitate recognition of contamination by melt during the LA-ICP-MS analyses of minerals.

Arc magmas typically contain 2–6 wt % H_2O (Sisson & Layne, 1993) and up to 12 wt % H_2O in evolved melts has been reported by Krawczynski *et al.* (2012). In this study, 3·0–13·5 wt % H_2O was added to the starting samples to investigate the effect of H_2O on the Nb and Ta partitioning.

Experimental pressures and temperatures

In hydrous basalt systems, amphibole is stable at pressures of up to 2·0–2·5 GPa and temperatures of up to 1000–1100°C, mainly depending on the H_2O and alkali (Na_2O and K_2O) contents of the bulk composition (Schmidt & Poli, 1998). In this study, experimental pressures of 0·5–2·0 GPa and temperatures of 850–1010°C were chosen to represent conditions in the middle to lower crust, with most experiments conducted at 1·0 GPa, the typical pressure of the arc crustal root. These *P–T* conditions are between the liquidus and solidus of the compositions studied and were expected to produce amphibole-bearing assemblages plus andesitic to felsic melts.

Experimental procedures

The sample containers were pure Au capsules (3 mm OD and 6 mm length). About 10 mg starting glass powder plus H_2O was enclosed in each capsule (H_2O was injected into the capsule with a micro-syringe before the powder was loaded into it). The capsules were welded shut with a precision welding machine (LAMPERT PUK U3) and were checked by drying–weighing to ensure no H_2O leakage. The experiments were performed on a Rockland piston-cylinder apparatus using assemblies consisting of graphite furnace ± Pyrex glass + talc sleeve + MgO inserts. Experiments at 1·5 and 2·0 GPa were conducted with ½ inch assemblies and those at 0·5 and 1·0 GPa were performed with ¾ inch assemblies. For the former, single-capsule setups were used, but for the latter, usually 2–4 sample capsules were mounted into an MgO cylinder at the center of the furnace. Such multi-capsule setups allow an excellent comparison of the results between samples with identical *P–T* conditions but different H_2O contents or starting compositions.

The experimental oxygen fugacities (fO_2) were not buffered, but were controlled by the initial Fe^{3+}/Fe^{2+} ratio + H_2O content of each sample and the fH_2 imposed by the assembly. The assemblies used here usually result in fO_2 in the hydrous samples being slightly higher than FMQ + 2, where FMQ is fayalite–magnetite–quartz buffer (Pichavant *et al.*, 2002; Liu *et al.*, 2014), corresponding to relatively oxidizing conditions. The specific fO_2 for a sample can be estimated with a mineral assemblage oxygen barometer if suitable phases are present in the run products (see section on 'Oxygen fugacities of the samples'). One run (NT-50) was conducted with a graphite-lined Au capsule to impose a very reducing fO_2 on the sample to check whether or not fO_2 has an effect on the Nb and Ta partitioning.

Pressure corrections of +13% and 0% were applied for the ½ and ¾ inch assemblies, respectively [see Liu *et al.* (2015) for the correction methods]. During an experiment, pressure was automatically regulated to the set-point. Temperature was measured and controlled using Pt–Pt90Rh10 (S-type) thermocouple to within ±2°C of the set-point using a Eurotherm controller, with no pressure correction applied to the thermocouple readings. The experiments lasted 48–164 h, which are longer than required to achieve equilibrium, as found by the previous similar study of Tiepolo *et al.* (2000). The recovered capsules after quenching were

Table 1: Starting compositions (quenched glasses)

	MKB-0	MKB-0.3	MKB-0.6	MKB-1.2	XT168N	Basanite
SiO_2	53·00(0·18)	51·62(0·20)	51·95(0·39)	52·14(0·32)	49·28(0·21)	44·82
TiO_2	0·01(0·02)	0·27(0·02)	0·57(0·03)	1·17(0·06)	1·68(0·06)	2·50
Al_2O_3	16·34(0·12)	15·96(0·09)	15·88(0·08)	16·07(0·08)	16·36(0·14)	14·73
FeO_t	12·70(0·01)	12·88(0·01)	12·43(0·02)	12·52(0·02)	11·33(0·33)	11·07
MnO	—	—	—	—	0·33(0·04)	0·19
MgO	6·19(0·05)	6·05(0·09)	5·90(0·08)	5·93(0·10)	7·27(0·07)	9·69
CaO	7·94(0·05)	7·91(0·14)	7·88(0·05)	7·91(0·08)	6·81(0·04)	10·05
Na_2O	2·97(0·05)	2·82(0·05)	2·83(0·05)	2·89(0·09)	3·91(0·03)	4·01
K_2O	0·80(0·03)	0·79(0·04)	0·80(0·03)	0·79(0·02)	1·42(0·03)	1·85
P_2O_5	—	—	—	—	0·37(0·03)	0·94
Total	99·95(0·25)	98·32(0·43)	98·25(0·22)	99·44(0·65)	98·38(0·50)	99·85
Mg#	47	46	46	46	54	61
Nb	93·16(0·49)	91·86(0·36)	92·76(0·29)	93·92(0·44)	118·42(0·67)	
Ta	215·73(1·30)	189·68(0·67)	205·18(1·19)	116·39(0·66)	95·13(0·51)	
Cs	87·07(0·64)	91·21(0·67)	95·66(0·87)	118·18(0·76)	225·63(1·04)	

Major element oxides (wt %, $n = 10$) were determined by EMPA. Nb, Ta and Cs (ppm, $n = 4$) were determined by LA-ICP-MS. Numbers in parenthesis are analytical uncertainties of 1σ standard deviations. Mg# = 100MgO/(MgO + FeO_t), molar. The data for basanite from Adam *et al.* (1993) are shown for comparison.

sectioned, mounted in epoxy and polished for optical observations and microbeam analyses.

Analytical methods

Major elements (wt %) in minerals and quenched melts were measured with a JEOL JXA-8230 electron microprobe. Silicate minerals were used as standards, with a ZAF matrix correction applied. Analytical conditions were 15 kV accelerating voltage, 20 nA beam current and 1 μm diameter beam for minerals, and 15 kV, 10 nA and 20 μm for quenched melts. A dry glass XT168, which was repeatedly analyzed by Xiong *et al.* (2005) and Liu *et al.* (2015), was used as a secondary standard to monitor analytical accuracy. Analytical precision is better than ±2% relative for SiO_2, Al_2O_3 and CaO, and ±5% for TiO_2, FeO, MnO, MgO and K_2O.

To obtain the phase proportions in the run products and to check for Fe loss during the experiments and Na loss during the analyses, mass-balance calculations between run products and starting composition were performed. The results revealed little (<5 wt % relative) or no Fe loss, but some Na loss in hydrous glasses. The reported Na_2O contents of the product glasses are the calibrated values from these calculations. The calibrated Na_2O contents in hydrous glasses appear to be accurate. This is confirmed by the LA-ICP-MS analyses of Na_2O, which show generally identical results within < ±5% relative compared with values obtained by electron microprobe analysis (EMPA), except for two samples with 10–20% relative errors (Fig. 3).

Trace elements Nb, Ta and Cs (ppm) in minerals and quenched melts were determined with the latest generation of LA-ICP-MS system (a Resolution S155 Resonetic 193 nm ArF excimer laser attached to an Agilent 7900a ICP-MS instrument) at the Guangzhou Institute of Geochemistry. ^{93}Nb, ^{181}Ta and ^{133}Cs were the analyzed isotopes; the major elements ^{23}Na, ^{25}Mg, ^{28}Si, ^{27}Al, ^{39}K, ^{43}Ca, ^{49}Ti, ^{55}Mn and ^{57}Fe were also analyzed. Helium was used as the carrier gas and N_2 was

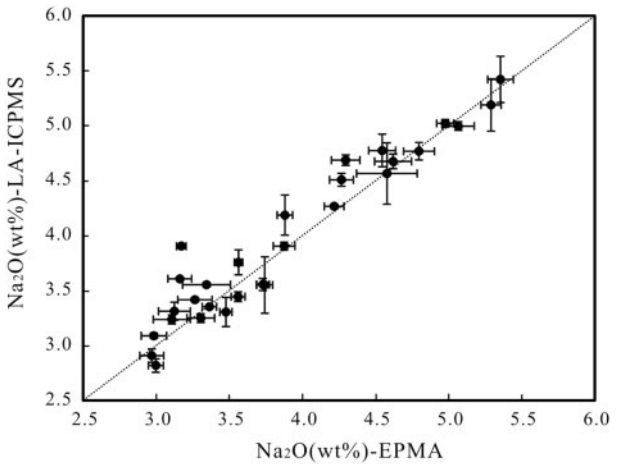

Fig. 3. Na_2O (wt %) calibrated by mass balance vs Na_2O (wt %) obtained by LA-ICP-MS for the quenched glasses, showing that Na_2O contents obtained by both methods are generally identical within less than ±5% relative error.

added to optimize detection limits. The operation conditions of the laser were 6–8 Hz frequency and 80 mJ energy. The laser spots were positioned over crystal-free pools of glass and at the rims of crystals when the mineral grains were sufficiently large. Spot sizes were mostly 13–25 μm for minerals and 19–56 μm for glasses. However, we had to use a 6 μm spot to analyze minerals and melt (glass) pools less than 10 μm across. The contrast in Nb and Ta analyses obtained using 6 μm and larger spots for amphibole, glass and the SRM 612 standard is shown in Table 2. The results indicate that the Nb and Ta analyses obtained with 6 μm spot are identical within error to those obtained with larger spots, except for the analyses with a 6 μm spot on two glass samples (NT107 and NT02) that show an ~10% relative error. The results obtained with a 6 μm spot are thus acceptable. NIST SRM 610 glass was used as the external standard and Al (amphibole, cpx, garnet) and

Table 2: Contrast of LA-ICP-MS Nb and Ta analyses obtained between 6 μm and larger spots

Sample no.	Spot size	Integration	*n*	Sample (ppm)		Standard (ppm)			
	(μm)	time (s)		Nb	Ta	610Nb	610Ta	612Nb	612Ta
NT107 melt	29	20	5	136(2)	163(4)	425(1)	454(1)	35(0)	38(0)
NT107 melt	13	26	5	135(3)	150(6)	425(2)	454(5)	35(1)	38(1)
NT107 melt	6	7	6	153(9)	176(10)	426(22)	456(6)	35(3)	36(1)
NT99 amp	13	26	9	26(3)	38(7)	425(5)	454(4)	34(0)	38(1)
NT99 amp	6	7	3	26(3)	34(3)	425(10)	457(22)	35(5)	39(2)
NT99 melt	32	26	3	114(1)	128(2)	425(4)	454(5)	35(1)	37(0)
NT99 melt	6	7	4	113(9)	133(4)	425(17)	457(32)	34(3)	34(2)
NT02 melt	25	30	3	134(1)	273(5)	425(1)	455(1)	34(0)	37(0)
NT02 melt	6	7	2	145(2)	308(3)	428(29)	454(13)	34(1)	39(2)
Reference values of the standards						419	456	38	39

Reference values of the standards from Gagnon *et al.* (2008); amp, amphibole.

Mg (olivine, opx and oxides) determined by EMPA were used as internal standards (Liu *et al.*, 2008). The reproducibility (1σ) of the measured Nb and Ta is <5% relative in the SRM 612 monitor standard. During the analysis, both accuracy and reliability of Nb and Ta analyses were also monitored using the time-resolved signals of Cs and Ti. Cs is strongly incompatible in the minerals produced in this study and thus contamination from melt inclusions can easily be recognized if Cs signals are elevated. Signals of Ti were used as an indicator of overprinting from Ti-oxides. Analyses were discarded if any contamination from melt or tiny Ti-oxides was evident.

EXPERIMENTAL RESULTS

Run products and phase relationships

A total of 36 samples were successfully synthesized, including 25 from the mid-K basalt (MKB) experiments and 11 from the high-K basalt (XT168N) experiments. The experimental conditions and results are listed in Table 3.

The MKB experiments were conducted at 0·5–2·0 GPa, 850–1010°C and 3·3–13·5 wt % H_2O. The degree of crystallinity in the run products ranges from 25 to 77 wt %; crystalline phases include amphibole, oxides, olivine, clinopyroxene, orthopyroxene, garnet and plagioclase. Phase relationships are shown in Fig. 4. Olivine was present only in the 0·5 GPa runs, garnet in the ≥1·5 GPa runs and plagioclase in the ≤1·5 GPa runs. Except for two runs, amphibole was the dominant crystalline phase (especially in the runs at low temperatures and low H_2O contents), making up 30–90 wt % in the crystalline assemblages (Table 3). Oxides, including magnetite, Ti-magnetite and spinel, were also widely present. They generally formed <10 μm subhedral to euhedral crystals. The amphibole was euhedral or subhedral with size of up to 80 μm. H_2O promoted crystal growth (Fig. 5) and had a strong effect on phase relationships, phase proportions and degree of crystallinity. It reduced the temperature of amphibole stability and led to the stability boundary of plagioclase moving to lower pressure and temperature (Fig. 4). Variations in the proportions of amphibole and oxides, degree of crystallinity and melt fraction with H_2O content are nearly linear. As shown by the multi-capsule experiments (bulk composition–*P*–*T* fixed; Fig. 6), amphibole proportion and crystallinity decrease, whereas the proportion of oxides and melt fraction increase with increasing melt H_2O content.

The XT168N experiments were conducted at 0·5 and 1·0 GPa, 900–1010°C and 3·0–10 wt % H_2O. These experiments have degrees of crystallinity ranging from 17 to 59 wt %. Crystalline phases include amphibole, oxides and olivine; plagioclase, orthopyroxene and clinopyroxene were absent for this composition under the experimental conditions. Amphibole was the dominant crystalline phase in all the runs; magnetite was generally present in the 1·0 GPa runs, but olivine and spinel were observed only in the 0·5 GPa runs. Variation trends for the proportions of amphibole and oxides, degree of crystallinity and melt fraction with melt H_2O content (Fig. 6c and d) are similar to those (Fig. 6a and b) in the MKB experiments. At similar experimental conditions, this high-K basalt composition always produced larger amphibole crystals than the mid-K basalt compositions. However, it is very difficult to produce amphibole crystals large enough (>15 μm) for LA-ICP-MS analysis from both the mid-K and high-K basalt compositions at low H_2O contents (<5·0 wt %) and low temperatures (≤900°C).

Oxygen fugacities of the samples

All except for four samples contain oxide ± olivine. Specific fO_2 values for these samples were calculated using mineral oxygen barometers. The fO_2 values of the samples containing olivine + spinel (six samples) were calculated using the olivine–spinel oxygen barometer of Ballhaus *et al.* (1991), whereas those of the samples containing spinel or magnetite in the absence of olivine were calculated from the melt Fe^{3+}/Fe^{2+} ratios (Kress & Carmichael, 1991), which were obtained from spinel (magnetite)–melt equilibria (Maurel & Maurel, 1982;

Table 3: Experimental conditions and results

Sample	Starting material	*P* (GPa)	*T* (°C)	Ini. H_2O (wt %)	Duration (h)	Run products and phase proportions (wt %)[a]										Fe loss[b] (wt % rel)	ΣR^{2c}	fO_2[d] (ΔFMQ)	amp in CA[e] (wt %)	oxide in in CA[f] (wt %)
						amp	mag	Ti-mag	spl	ol	opx	cpx	gt	pl	glass					
Starting composition: mid-K basalts (MKB)																				
NT19	MKB-0.3	2	950	7·9	144	—	—	—	—	—	—	20	33	—	47	1·0	0·03			
NT35	MKB-0.6	2	850	4·5	140	65	—	—	—	—	—	—	1	—	34	0·0	2·25		98	
NT46	MKB-0.6	1·5	1010	7·1	80	13	—	—	1·5	—	1	12	—	—	72	0·0	0·45	–1·40	46	5
NT17	MKB-0.3	1·5	950	7·2	134	40	4·7	—	—	—	—	1·3	—	—	54	0·0	0·27	3·35	87	10
NT33	MKB-0.6	1·5	850	4·3	143	65	—	—	—	—	—	—	1	3	31	0·0	0·71		94	
NT57	MKB-0.6	1·0	1010	13·5	52	—	16	—	—	—	2	25	—	—	57		1·66	3·03		37
NT123	MKB-1.2	1·0	1010	5·0	47	8	8	—	—	—	3	9	—	—	72	0·9	0·07	3·14	29	29
NT48	MKB-0.6	1·0	1010	7·5	73	9·6	—	—	1·6		2·8	9·5	—	—	76	0·0	0·97	0·86	40	7
NT50	MKB-0.6	1·0	1010	7·3	72	15	—	—	0·1		7·7	6·3	—	—	71	0·9	0·91	–6·07	52	<1
NT05	MKB-1.2	1·0	950	7·7	144	24	4	—	—	—	—	—	—	—	72	0·0	0·21	3·14	86	14
NT06	MKB-0.6	1·0	950	7·5	144	30	2	—	—	—	—	1	—	—	67	0·0	0·44	2·87	91	6
NT07	MKB-0.3	1·0	950	7·6	144	27	4	—	—	—	—	—	—	—	69	0·0	0·05	3·13	87	13
NT08	MKB-0.0	1·0	950	7·6	144	30	3	—	—	—	—	—	—	—	67	0·0	0·16	3·35	91	9
NT97	MKB-1.2	1·0	950	4·3	89	34	6	3	—	—	—	—	—	22	35	0·0	0·66	3·88	52	14
NT98	MKB-1.2	1·0	950	5·5	89	32	6	3	—	—	—	—	—	15	44	0·0	0·81	3·88	57	16
NT99	MKB-1.2	1·0	950	8·5	89	19	5	5	—	—	—	3	—	—	66	0·0	0·47	4·33	56	29
NT104	MKB-1.2	1·0	900	3·3	136	44	6	—	—	—	—	—	—	20	30	0·5	0·56	2·35	63	9
NT105	MKB-1.2	1·0	900	4·2	136	42	6	—	—	—	—	—	—	9	43	0·9	0·60	2·11	74	11
NT106	MKB-1.2	1·0	900	5·7	136	39	6·5	—	—	—	—	—	—	4·5	50	0·6	0·30	2·41	78	13
NT107	MKB-1.2	1·0	900	8·1	136	30	8	—	—	—	—	—	—	—	62	1·1	0·59	2·58	79	21
NT42	MKB-0.6	1·0	850	4·6	145	43	9	—	—	—	—	—	—	25	23	0·0	2·42	4·37	56	11
NT01	MKB-1.2	0·5	950	6·1	164	24	5	—	—	—	—	—	—	—	71	1·6	0·29	3·06	83	17
NT02	MKB-0.6	0·5	950	4·9	164	18	5·2			3	3			5·4	65·4	0·84	0·0	3·50	52	15
NT03	MKB-0.3	0·5	950	4·7	164	24	5	—	—	1	—	4	—	4	62	0·0	0·03	3·49	71	15
Starting composition: high-K basalt (XT168N)																				
NT121	XT168N	1·0	1010	5·2	47	32	6	—	—	—	—	—	—	—	62	0·0	0·92	3·10	84	16
168-4b	XT168N	1·0	950	5·5	168	40	6	—	—	—	—	—	—	—	54	0·0	0·76	4·0	87	13
NT100	XT168N	1·0	950	3·0	97	59	tr	—	—	—	—	—	—	—	41	0·0	1·72		100	<1
NT101	XT168N	1·0	950	3·7	97	45	4	—	—	—	—	—	—	—	51	0·0	0·11	2·35	92	8
NT102	XT168N	1·0	950	4·9	97	39	5	—	—	—	—	—	—	—	56	0·0	0·13	2·56	89	11
NT103	XT168N	1·0	950	7·1	97	31	6	—	—	—	—	—	—	—	63	0·0	0·89	2·55	84	16
NT116	XT168N	1·0	900	6·3	107	41	4	4	—	—	—	—	—	—	51	0·0	0·49	3·71	84	16
NT72	XT168N	0·5	950	5·9	106	13	—	—	3	9	—	—	—	—	75	4·2	0·76	1·28	52	12
NT73	XT168N	0·5	950	7·2	106	6·5	—	tr	2·5	8·5	—	—	—	—	82·5	0·3	0·26	2·09	39	14
NT74	XT168N	0·5	950	8·8	106	6	—	3		8	—	—	—	—	83	0·8	0·46	3·45	35	18
NT75	XT168N	0·5	950	9·2	106	4	—	—	4	9	—	—	—	—	83	1·4	0·35	1·81	24	24

All the experiments were carried out in a pure Au capsule, except for NT-50, which was conducted with a graphite-lined Au capsule. Samples with the same *P*, *T* and duration were run simultaneously in the same experiment.

[a]Phase proportions calculated by mass balance using EMPA data (amp, amphibole; ol, olivine; opx, orthopyroxene; cpx, clinopyroxene; gt, garnet; pl, plagioclase; mag, magnetite; Ti-mag, Ti-magnetite; spl, spinel; glass, quenched melt).

[b]FeO loss relative expressed as $100(FeO_{calc} - FeO_{starting\ glass})/FeO_{starting\ glass}$ with FeO_{calc} from mass-balance calculation.

[c]Sum of the square of the residuals with SiO_2, TiO_2, Al_2O_3, MgO, CaO and K_2O. ΣR^2 values in four samples are >1·0 because of significant H_2O loss in these samples during the experiments, leading to lower accuracy of the calculated results.

[d]fO_2 values at *P* and *T*. For the samples containing olivine and spinel, fO_2 values were calculated from olivine–spinel equilibria (Ballhaus *et al.*, 1991); for olivine-free but Cr–Al spinel-bearing samples, fO_2 values were calculated from spinel–liquid equilibria (Maurel & Maurel, 1982; Kress & Carmichael, 1991; Danyushevsky & Sobolev, 1996) (see text for details).

[e]Amphibole total (wt %) in the crystalline assemblage.

[f]Oxide total (wt %, magnetite + Ti-magnetite + spinel) in the crystalline assemblage.

Danyushevsky & Sobolev, 1996). Spinel and magnetite are solid solutions and thus the oxide ± olivine oxygen barometers are expected to be applicable across the entire spectrum of spinel-group compositions and give reasonable results for temperatures as low as 800°C (Ballhaus *et al.*, 1991). The calculated results (Table 3) show that fO_2 in most of the samples was between FMQ + 1 and FMQ + 4. Such an fO_2 range and the wide presence of magnetite indicate oxidizing conditions in the samples, consistent with the redox environment of arc magmatic systems. NT-50 was a run conducted with a graphite-lined Au capsule. The fO_2 of this sample obtained from the spinel–melt equilibrium is FMQ–6·1 (Table 3). With this very reducing fO_2 value, the Fe^{3+}/Fe^{2+} ratio in the melt should be zero. This is in agreement with the chemical analysis of the spinel from this sample, which shows no Fe^{3+} present (Supplementary Data Table S4), indicating no Fe^{3+} present in the melt.

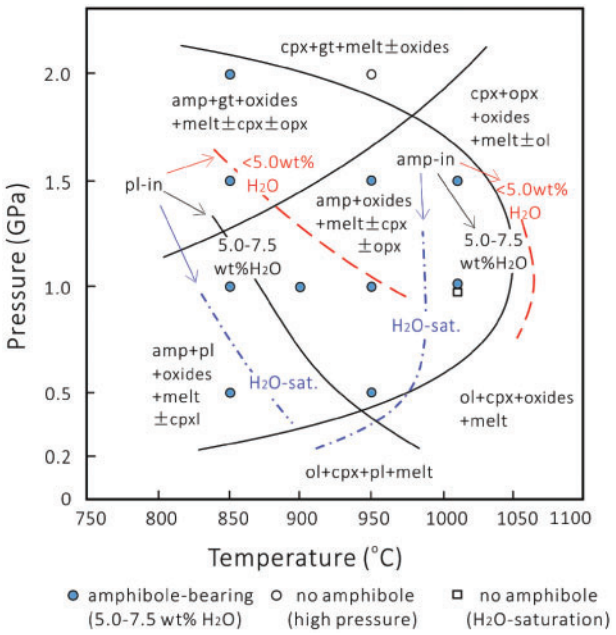

Fig. 4. Phase relationships for the MKB composition system (0·5–2·0 GPa, 850–1010°C and 3·0–13·5 wt % bulk H_2O content), showing that H_2O reduces the temperature of amphibole stability and leads to the plagioclase stability boundary moving to lower pressure and temperature. Mineral abbreviations as in Table 3.

Melt composition and H_2O content

The melts generally quenched to clear glasses and quench crystals were rarely found. Major element oxides (EMPA, normalized to 100% anhydrous) and Nb, Ta and Cs contents (LA-ICP-MS) are reported in Table 4. All the melts are compositionally homogeneous. Melt composition is a function of bulk composition, *T*, *P* and H_2O. The melts derived from the MKB compositions are andesitic to rhyolitic with SiO_2 ranging from 55·5 to 75·7 wt % and Mg# from 23 to 54; those derived from the XT168N composition are basaltic andesitic to dacitic with SiO_2 ranging from 53·3 to 64·3 wt % and Mg# from 32 to 57. The polymerization degree of the melt is usually expressed as the NBO/T ratio. However, owing to the lack of data on Fe^{3+}/Fe^{2+} ratios and H-speciation in our melts, which are needed to correctly calculate

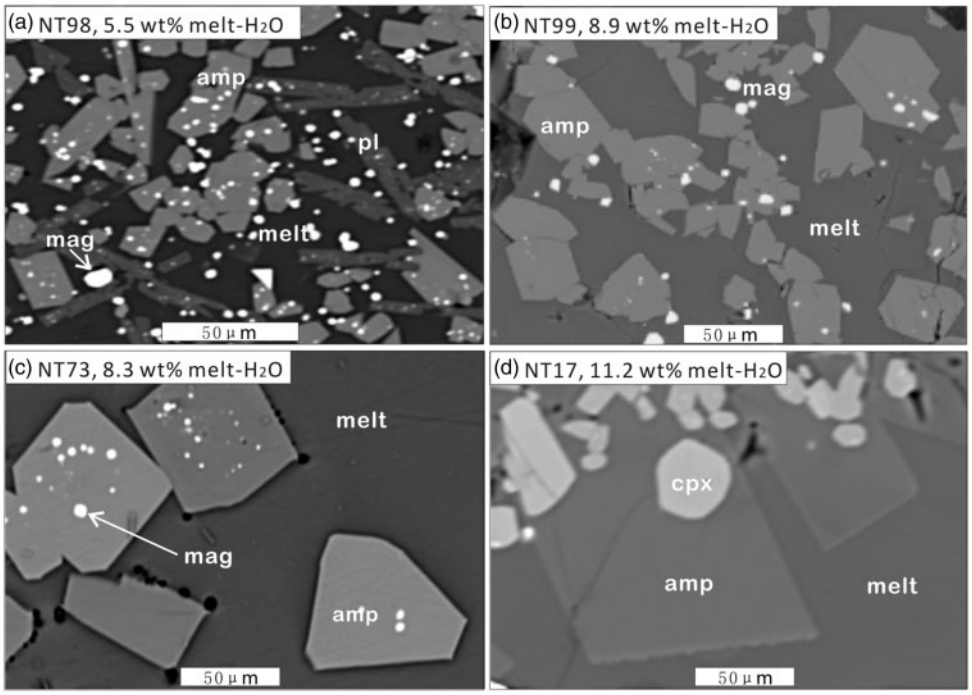

Fig. 5. Representative run products (experimental conditions in Table 3) showing that (1) quenched melts are clean and amphiboles (amp) are euhedral to subeuhedral, and (2) the size of amphibole crystals increases generally with increasing melt H_2O content.

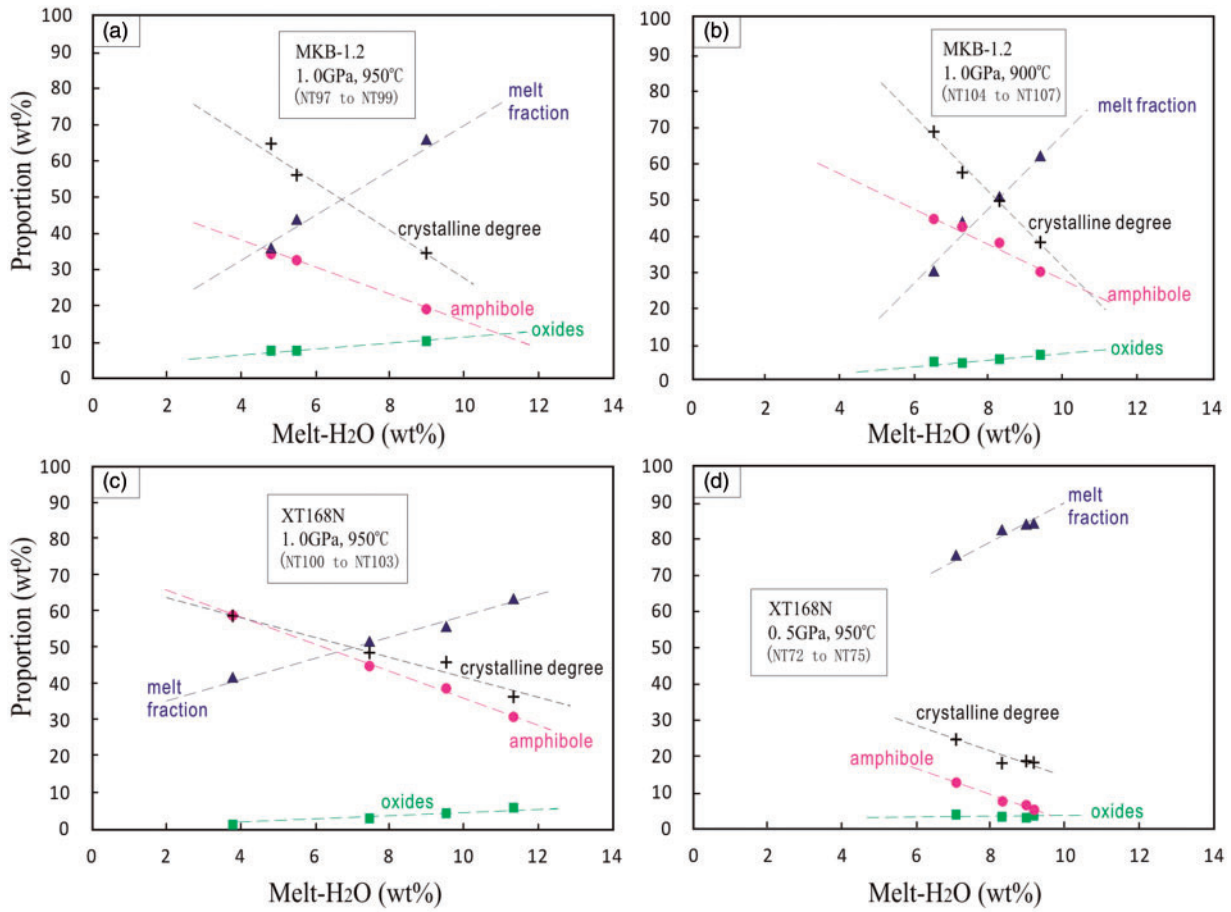

Fig. 6. Variations in the proportion (wt %) of amphibole, oxides (magnetite + Ti-magnetite + spinel), degree of crystallinity and melt fraction with melt H_2O content (wt %) in the multi-capsule experiments, showing that amphibole and crystalline degree decrease whereas oxides and melt fraction increase with increasing melt H_2O content. Data from Table 3.

NBO/T, we here neglect Fe^{3+} and H-speciation and use X_{nf}/X as a rough expression for the melt polymerization. X_{nf}/X is defined as the sum of the molar fractions of network-forming cations (i.e. Si and the fraction of Al that is balanced by Na and K) normalized to the sum of the molar fractions of all the cations in the anhydrous melt (Nielsen, 1990). The X_{nf}/X values of MKB-derived melts are 0·58–0·80 and those of XT168N-derived melts are 0·59–0·71 (Table 4).

All the melts were H_2O-undersaturated except for three runs (NT57, NT74 and NT75) that contain fluid bubbles in the quenched glasses, indicating H_2O saturation. Two methods were used to obtain melt H_2O content. One was to calculate the H_2O content by the difference of the EMPA total from 100%. The other was to estimate it by mass balance, where H_2O_{melt} = [(initial H_2O – amphibole H_2O)/melt mass], with 2 wt % H_2O in amphibole assumed. By comparison, 70% of the samples show that the two methods yielded identical H_2O contents with absolute differences between them of $\leq \pm 1{\cdot}0$ wt % (Table 4), but ~30% of the samples show that H_2O_{melt} (by difference) is lower than H_2O_{melt} (mass balance), with absolute differences between them $>1{\cdot}0$ wt %. For these samples, the H_2O decrease (by difference compared with mass balance) would be due to (1) H_2O loss during the experiments (H_2 diffused out from the capsule, resulting in H_2O loss in the sample, (2) H_2O saturation, such as in the three runs mentioned above, or (3) potential uncertainties of amphibole H_2O estimation for the calculations of mass balance.

Measuring H_2O content by difference for glasses containing >1 wt % H_2O has proved to be accurate. The results obtained by this method were comparable with the values obtained by microanalytical methods such as Fourier transform infrared spectrometry and secondary ion mass spectrometry (e.g. Devine *et al.*, 1995; Morgan & London, 1996; Melekhova *et al.*, 2013), although the microanalytical methods are more sensitive for glasses with low H_2O contents. We believe that our results obtained from the 'by difference' method are also reliable and accurate, as the melt Na_2O values were calibrated and the analyses of other oxides are accurate. The 'by difference' melt H_2O contents (3·80–12·51 wt %, Table 4) are thus representative of the true values, and are used to discuss the effect of melt H_2O content in subsequent sections.

Table 4: Compositions and Nb and Ta analyses of the melts

Sample	NT19	NT35	NT46	NT17	NT33	NT57	NT123	NT48	NT50	NT05	NT06	NT07
SiO_2	62·33(46)	76·52(73)	56·25(20)	65·18(39)	74·22(54)	68·74(40)	59·34(24)	55·46(19)	55·54(11)	58·98(41)	59·00(19)	59·27(45)
TiO_2	0·24(3)	0·12(2)	0·51(1)	0·15(1)	0·12(7)	0·50(4)	0·77(3)	0·53(3)	0·59(4)	0·60(3)	0·28(3)	0·16(3)
Al_2O_3	16·72(25)	15·96(17)	18·43(6)	17·96(25)	14·93(14)	17·50(15)	18·72(7)	18·13(12)	18·81(4)	18·00(15)	17·89(8)	18·25(11)
FeO	5·79(43)	1·69(18)	10·58(11)	4·34(46)	1·99(15)	4·54(17)	5·99(11)	10·94(23)	10·16(26)	7·56(27)	8·67(35)	7·81(28)
MnO	n.a.	n.a.	n.a.	n.a.	n.a.	n.a.	n.a.	n.a.	n.a.	n.a.	n.a.	n.a.
MgO	1·92(17)	0·28(2)	3·28(2)	1·57(28)	0·37(8)	1·58(6)	3·20(18)	3·51(7)	3·24(13)	3·10(10)	2·72(10)	2·77(8)
CaO	4·71(12)	1·30(4)	6·58(3)	5·94(19)	3·09(9)	4·88(12)	7·14(15)	7·22(13)	7·23(19)	7·57(12)	7·16(17)	7·49(10)
Na_2O[a]	5·51(14)	2·81(3)	3·44(4)	3·68(13)	3·57(4)	4·89(8)	3·69(4)	3·39(9)	3·56(17)	3·33(6)	3·27(9)	3·33(10)
K_2O	2·75(26)	1·30(67)	1·07(3)	1·15(5)	1·67(4)	1·50(6)	0·78(4)	1·03(6)	1·00(11)	0·85(6)	0·94(6)	0·91(8)
P_2O_5	n.a.	n.a.	n.a.	n.a.	n.a.	n.a.	n.a.	n.a.	n.a.	n.a.	n.a.	n.a.
Total	92·11(105)	87·49(13)	91·69(23)	88·76(84)	89·60(0)	90·37(51)	94·17(12)	92·54(29)	93·99(39)	90·12(52)	90·88(42)	89·65(48)
Na_2O[b]			3·90(1)	3·42(2)			3·31(13)	3·61(1)	3·55(2)	2·82(6)	2·91(6)	3·09(2)
Na_2O(rel)[c]			–20·25%	–4·49%			5·18%	–14·10%	–5·75%	6·34%	2·12%	–3·41%
H_2O[d]	7·89/16·72	12·51/9·47	8·31/9·40	11·24/11·78	10·40/9·90	9·63/31·39	5·84/6·65	7·46/9·48	6·01/6·91	9·88/10·08	9·12/10·27	10·35/10·15
X_{nf}/X^e	0·70	0·79	0·60	0·69	0·78	0·71	0·63	0·59	0·59	0·62	0·62	0·62
Mg#	37(4)	23(3)	36(0)	39(9)	25(0)	39(2)	49(3)	37(1)	36(2)	42(2)	36(2)	39(2)
PS (μm)[f]	29	6	56	25	6		13*	56	56	25	25	25
Nb	176(3)	110(7)	136(2)	137(0)	154(1)		125(6)	131(3)	134(2)	107(1)	130(3)	106(1)
Ta	350(24)	319(48)	263(6)	276(8)	483(6)		151(8)	245(9)	251(3)	126(3)	281(4)	211(2)
Cs	318(50)	147(23)	128(1)	146(2)	248(22)		154(7)	117(1)	117(1)	142(10)	128(7)	115(2)

Sample	NT08	NT97	NT98	NT99	NT104	NT105	NT106	NT107	NT42	NT01	NT02	NT03
SiO_2	59·97(27)	69·47(25)	68·65(22)	62·17(27)	71·45(21)	69·62(47)	67·26(29)	63·52(43)	75·69(122)	59·83(64)	60·52(74)	60·89(54)
TiO_2	0·01(1)	0·22(3)	0·25(3)	0·26(3)	0·26(1)	0·25(2)	0·33(2)	0·49(3)	0·09(4)	0·52(3)	0·32(2)	0·12(2)
Al_2O_3	18·50(16)	16·99(5)	17·11(7)	19·51(11)	15·75(8)	16·71(8)	17·76(9)	19·32(18)	14·14(51)	18·31(25)	18·34(17)	18·45(16)
FeO	7·86(32)	2·24(10)	2·61(10)	3·45(13)	2·48(7)	3·07(15)	3·23(8)	3·80(6)	1·46(8)	6·61(32)	6·63(32)	6·41(18)
MnO	n.a.	n.a.	n.a.	n.a.	n.a.	n.a.	n.a.	n.a.	n.a.	n.a.	0·02(1)	n.a.
MgO	2·23(19)	1·42(2)	1·63(3)	2·71(11)	0·77(2)	0·77(5)	1·03(3)	1·51(7)	0·64(8)	3·12(14)	2·79(16)	2·41(15)
CaO	7·21(17)	3·74(12)	4·42(12)	7·19(7)	3·51(9)	4·14(11)	5·27(6)	6·72(10)	2·13(2)	7·15(17)	6·58(12)	6·24(12)
Na_2O[a]	3·47(12)	4·15(6)	3·77(3)	3·69(5)	3·99(5)	4·00(6)	3·87(5)	3·65(10)	3·61(15)	3·39(14)	3·64(8)	4·20(8)
K_2O	0·69(7)	1·96(4)	1·53(3)	0·98(5)	1·77(3)	1·40(5)	1·23(3)	0·96(2)	2·23(4)	1·03(5)	1·14(7)	1·22(4)
P_2O_5	n.a.	n.a.	n.a.	n.a.	n.a.	n.a.	n.a.	n.a.	n.a.	n.a.	0·00(0)	n.a.
Total	89·89(43)	95·15(27)	94·56(30)	91·11(27)	93·49(19)	92·65(24)	91·89(39)	90·49(73)	94·87(168)	91·53(70)	91·72(44)	92·21(37)
Na_2O[b]	3·31(8)	4·22(18)	3·76(11)	3·35(1)	3·56(5)	3·55(26)	3·44(4)	3·25(4)		3·24(4)	3·58(4)	3·90(4)
Na_2O(rel)[c]	–5·70%	–6·40%	–5·17%	0·34%	4·87%	4·39%	3·36%	1·67%		–4·05%	–6·90%	–0·77%
H_2O[d]	10·11/10·52	4·85/10·25	5·45/10·71	8·89/11·94	6·51/7·91	7·35/8·09	8·11/9·01	9·51/11·94	5·13/16·67	8·47/7·88	8·28/6·89	7·79/6·85
X_{nf}/X^e	0·63	0·74	0·72	0·65	0·76	0·74	0·71	0·67	0·80	0·63	0·64	0·65
Mg#	34(3)	53(2)	53(2)	59(3)	36(1)	31(3)	37(2)	42(2)	44(7)	46(3)	0·43(3)	40(3)
PS (μm)[f]	25	13*	13	32	13	13*	13	13	29*	25	25	25
Nb	108(2)	181(9)	140(6)	114(0)	162(2)	147(12)	151(1)	135(3)	119(3)	109(1)	134(1)	117(1)
Ta	248(2)	215(12)	170(5)	128(2)	221(2)	195(16)	185(0)	150(6)	307(9)	132(6)	273(5)	235(5)
Cs	109(3)	306(16)	236(15)	161(1)	333(8)	269(21)	228(4)	177(8)	301(3)	157(1)	128(2)	132(3)

(continued)

Table 4: Continued

Sample	NT121	168-4b	NT100	NT101	NT102	NT103	NT116	NT72	NT73	NT74	NT75
SiO_2	57·90(90)	61·31(30)	61·59(43)	61·26(17)	60·61(20)	59·63(120)	64·05(39)	54·81(12)	53·63(19)	53·31(22)	53·81(23)
TiO_2	0·96(5)	0·42(8)	0·44(2)	0·64(4)	0·75(4)	0·91(5)	0·27(2)	1·18(4)	1·44(6)	1·57(5)	1·51(3)
Al_2O_3	18·97(28)	19·24(14)	19·45(11)	19·51(5)	19·71(10)	19·87(33)	20·27(17)	19·54(9)	19·33(9)	19·55(16)	19·47(13)
FeO	5·89(21)	3·33(12)	5·61(14)	4·52(19)	4·66(11)	4·49(47)	1·72(3)	6·97(13)	7·50(15)	6·81(13)	7·09(12)
MnO	0·36(3)	0·29(2)	0·24(3)	0·26(2)	0·29(3)	0·33(4)	0·21(3)	0·33(4)	0·33(3)	0·32(2)	0·33(3)
MgO	3·36(28)	2·48(8)	1·49(8)	2·03(3)	2·27(6)	2·21(53)	1·28(8)	3·13(9)	3·57(5)	3·73(14)	3·57(7)
CaO	5·99(30)	5·04(5)	3·55(11)	4·28(6)	4·70(7)	6·19(10)	4·12(9)	6·81(8)	7·37(9)	7·94(10)	7·43(15)
Na_2O^a	4·89(22)	5·26(6)	5·55(9)	5·48(12)	5·30(12)	5·20(14)	5·71(7)	4·89(10)	4·68(11)	4·64(7)	4·69(9)
K_2O	1·01(19)	2·02(5)	2·07(35)	2·01(6)	1·71(10)	1·14(9)	1·97(5)	1·84(5)	1·63(5)	1·66(5)	1·65(7)
P_2O_5	0·47(7)	0·59(3)	0·63(6)	0·73(5)	0·67(4)	0·69(3)	0·38(3)	0·51(6)	0·48(4)	0·46(5)	0·43(4)
Total	93·53(70)	94·53(25)	96·20(47)	92·51(14)	90·47(20)	88·65(99)	92·55(49)	92·90(36)	91·69(34)	90·96(53)	90·93(43)
Na_2O^b	4·57(28)	5·02(3)	5·42(21)	5·00(4)	4·77(8)	4·67(7)	5·19(24)	4·77(15)	4·69(5)	4·27(2)	4·51(6)
$Na_2O(rel)^c$	0·08%	–0·89%	–1·21%	1·39%	0·62%	–1·18%	1·95%	–4·79%	–8·33%	–1·15%	–5·34%
H_2O^d	6·47/7·33	5·47/8·73	3·80/4·45	7·49/6·62	9·53/7·28	11·35/13·68	7·45/11·25	7·10/5·68	8·31/8·57	9·04/10·46	9·07/10·99
X_{nf}/X^e	0·63	0·68	0·69	0·68	0·67	0·65	0·71	0·61	0·60	0·59	0·60
Mg#	51(5)	57(3)	32(2)	45(2)	47(2)	47(14)	57(4)	45(2)	46(1)	50(2)	48(1)
PS (μm)^f	13*	25	13	13	13	32	13	19	19	19	19
Nb	156(10)	157(3)	146(3)	167(7)	164(3)	159(1)	156(9)	145(5)	147(3)	139(1)	145(3)
Ta	114(9)	123(7)	127(5)	132(5)	120(3)	117(1)	115(7)	113(3)	115(1)	110(2)	112(2)
Cs	341(19)	396(18)	504(2)	419(3)	373(7)	310(12)	373(43)	334(10)	315(3)	276(3)	300(9)

*Only one analysis was obtained.
Major element (wt %, $n = 6$–12) by EMPA normalized to 100% anhydrous, Nb, Ta and Cs (ppm, $n = 3$–6) by LA-ICP-MS. n.a., not analyzed. Numbers in parenthesis are 1σ standard deviations in terms of last unit cited [for example, 2·97(5) = 2·97 ± 0·05 and 7·57(108) = 8·97 ± 1·08]; standard deviation of Mg# was calculated by $SD_{Mg\#} = \{(SD_{Mg}/40)^2/(C_{Mg}/40 + C_{Fe}/72)^2 + [(SD_{Mg}/40)^2 + (SD_{Fe}/72)^2] \times (C_{Mg}/40)^2/(C_{Mg}/40 + C_{Fe}/72)^4\}^{0.5}$.
[a]Na_2O content calibrated by mass-balance calculation in anhydrous melt.
[b]Na_2O content obtained by LA-ICP-MS.
[c]Na_2O relative expressed as $(Na_2O^a \times Total - Na_2O^b)/Na_2O^b$.
[d]H_2O content (obtained by difference/obtained by mass balance).
[e]X_{nf}/X, the sum of the molar fractions of network-forming cations normalized to the sum of the molar fractions of all the cations in the melt.
[f]PS (μm), LA-ICP-MS spot size.

Table 5: Amphibole compositions and Nb, Ta and Ti partition coefficients

Sample	NT35	NT46	NT17	NT33	NT123	NT48	NT50	NT05	NT06	NT07	NT08
SiO_2	40·45(42)	42·27(45)	42·89(65)	40·92(9)	42·23(84)	41·49(33)	41·55(86)	43·35(30)	42·95(13)	43·96(58)	43·82(49)
TiO_2	1·12(61)	0·92(4)	0·41(3)	1·06(20)	1·92(12)	1·14(7)	1·67(11)	1·19(16)	0·67(8)	0·34(8)	0·02(4)
Al_2O_3	16·14(59)	14·37(56)	14·12(73)	16·25(23)	13·73(14)	13·99(58)	14·97(37)	12·61(19)	13·23(22)	12·56(33)	12·70(39)
FeO	18·62(121)	14·53(44)	13·59(43)	18·97(69)	10·54(9)	14·69(47)	13·48(34)	11·86(31)	14·21(35)	12·06(51)	12·63(79)
MnO	n.a.	n.a.	n.a.	n.a.	n.a.	n.a.	n.a.	n.a.	n.a.	n.a.	n.a.
MgO	8·96(169)	12·64(28)	12·41(56)	9·07(41)	14·63(22)	12·73(32)	12·34(37)	14·09(21)	12·72(12)	14·15(66)	13·97(57)
CaO	8·72(71)	9·58(54)	10·47(28)	8·81(17)	10·87(19)	9·93(9)	10·07(21)	11·18(21)	10·77(20)	11·13(25)	11·19(36)
Na_2O	2·86(32)	2·71(14)	2·21(7)	2·43(3)	2·29(6)	2·59(7)	2·50(6)	2·20(6)	2·24(12)	2·19(8)	2·21(10)
K_2O	0·53(17)	0·54(3)	0·47(6)	0·42(3)	0·37(2)	0·46(7)	0·46(4)	0·41(3)	0·41(2)	0·44(3)	0·43(3)
Total	97·41(8)	97·57(45)	96·56(106)	97·95(16)	96·61(72)	97·01(25)	97·05(126)	96·90(36)	97·22(59)	96·85(52)	96·99(83)
Mg#	46(10)	61(2)	62(4)	46(3)	71(1)	61(2)	62(3)	68(2)	62(1)	68(4)	67(4)
K_D^{Fe-Mg}	0·34(8)	0·36(1)	0·40(9)	0·38(2)	0·38(2)	0·37(2)	0·35(2)	0·34(2)	0·35(2)	0·30(2)	0·26(3)
PS (μm)	6	25	25*	6	13*	25	25	25	25	25	25
Nb	59(6)	26(2)	24(1)	139(15)	27 (1)	48 (5)	52(3)	27(1)	45(2)	26(1)	34(2)
Ta	87(17)	45(3)	35(1)	154 (32)	29(1)	93(10)	94(5)	28(1)	80(6)	49(2)	75(4)
Cs	0·51(23)	0·18(9)	0·16(4)	1·74(90)	6·97(277)	0·11(8)	0·32(10)	0·20(2)	0·10(5)	0·27(27)	0·28(35)
Nb/Ta	0·68(15)	0·57(6)	0·70(4)	0·90(21)	0·92(7)	0·52(8)	0·55(4)	0·94(5)	0·56(5)	0·53(3)	0·45(4)
D_{Nb}	0·54(6)	0·19(1)	0·18(1)	0·90(9)	0·22(2)	0·37(4)	0·38(2)	0·25(1)	0·35(2)	0·25(1)	0·32(2)
D_{Ta}	0·27(7)	0·17(1)	0·13(1)	0·32(7)	0·19(1)	0·37(4)	0·37(2)	0·23(1)	0·28(2)	0·23(1)	0·30(2)
D_{Nb}/D_{Ta}	1·97(53)	1·11(11)	1·41(9)	2·81(65)	1·11(8)	0·99(16)	1·03(8)	1·11(7)	1·21(11)	1·06(7)	1·04(10)
D_{Ti}	10·61(597)	1·97(10)	3·19(38)	10·23(193)	2·64(20)	2·33(19)	3·01(30)	2·20(31)	2·66(43)	2·44(74)	1·81(174)

Sample	NT97	NT98	NT99	NT104	NT105	NT106	NT107	NT42	NT01	NT02	NT03
SiO_2	42·90(70)	42·41(109)	42·53(46)	43·41(61)	42·32(57)	41·26(15)	43·17(93)	45·84(62)	41·98(37)	43·07(38)	43·25(37)
TiO_2	2·17(31)	2·08(21)	1·55(23)	1·63(10)	1·58(16)	1·67(8)	1·42(10)	1·09(24)	1·67(22)	0·99(18)	0·54(15)
Al_2O_3	12·21(18)	12·98(75)	13·14(32)	12·38(24)	13·57(47)	14·77(38)	12·93(92)	10·15(28)	12·91(50)	13·31(121)	12·03(36)
FeO	11·07(67)	11·54(105)	9·33(31)	13·98(67)	14·04(97)	13·67(68)	11·09(127)	13·27(81)	11·30(42)	11·54(122)	11·64(24)
MnO	n.a.	n.a.	n.a.	n.a.	n.a.	n.a.	n.a.	n.a.	n.a.	n.a.	n.a.
MgO	14·84(29)	14·50(21)	15·89(46)	13·33(58)	12·26(61)	12·23(54)	14·92(131)	14·99(48)	13·88(57)	13·41(80)	14·10(26)
CaO	10·61(31)	10·62(36)	11·61(57)	10·30(35)	10·76(18)	11·23(15)	11·33(27)	10·25(51)	11·48(12)	11·34(57)	11·14(28)
Na_2O	2·12(8)	2·09(18)	2·10(4)	1·85(6)	2·01(12)	2·09(9)	2·17(9)	1·75(6)	2·17(6)	2·23(6)	2·16(8)
K_2O	0·41(4)	0·33(3)	0·33(3)	0·36(2)	0·36(2)	0·39(2)	0·41(4)	0·31(4)	0·32(2)	0·33(4)	0·32(2)
Total	96·35(62)	96·57(63)	96·45(44)	97·06(79)	96·95(39)	97·32(50)	97·48(65)	97·64(50)	95·711(39)	96·20(11)	95·18(78)
Mg#	71(3)	69(3)	75(3)	63(4)	61(5)	62(4)	71(9)	67(4)	69(4)	68(5)	69(2)
K_D^{Fe-Mg}	0·47(4)	0·47(5)	0·46(3)	0·33(2)	0·29(3)	0·36(3)	0·30(4)	0·39(6)	0·38(3)	0·36(5)	0·31(2)
PS (μm)	6	13	13	6	6	13	13		25	25	25
Nb	106(4)	72(9)	26(3)	86(7)	59 (6)	59 (8)	23(4)		44(1)	90(5)	70(5)
Ta	98(1)	76(804)	38(7)	80 (12)	63 (9)	62 (61)	26(3)		50(2)	177(9)	124(10)
Cs	4·06(86)	1·57(87)	0·19(30)	0·97(94)	1·86(56)	0·64(58)	0·21(17)		0·20(12)	0·29(41)	1·98(112)
Nb/Ta	1·08(4)	0·95(16)	0·68(15)	1·07(18)	0·94(16)	0·95(16)	0·91(18)		0·89(4)	0·51(4)	0·56(6)
D_{Nb}	0·58(3)	0·52(7)	0·23(3)	0·53(4)	0·40(5)	0·39(5)	0·17(3)		0·40(1)	0·68(4)	0·60(4)
D_{Ta}	0·46(3)	0·45(5)	0·30(6)	0·36(5)	0·32(5)	0·34(3)	0·17(2)		0·38(2)	0·65(4)	0·53(4)
D_{Nb}/D_{Ta}	1·28(10)	1·15(20)	0·76(17)	1·46(25)	1·23(26)	1·17(19)	1·02(21)		1·07(7)	1·04(8)	1·14(12)
D_{Ti}	10·37(202)	8·74(147)	6·45(112)	6·52(52)	6·78(95)	5·53(43)	3·21(29)		3·50(52)	3·34(64)	4·93(163)

(continued)

Table 5: Continued

Sample	NT121	168N4b	NT100	NT101	NT102	NT103	NT116	NT72	NT73	NT74	NT75
SiO_2	41·74(12)	40·46(65)	40·67(45)	40·73(52)	41·03(33)	41·84(32)	41·61(81)	40·63(38)	41·07(33)	41·43(43)	41·02(27)
TiO_2	2·12(12)	1·39(15)	2·41(18)	2·32(6)	2·17(12)	1·83(7)	2·17(21)	3·35(38)	3·21(25)	3·47(15)	3·17(37)
Al_2O_3	13·32(8)	14·20(16)	14·86(7)	14·41(18)	14·14(21)	13·25(16)	13·63(100)	13·71(31)	13·19(27)	13·18(47)	13·26(45)
FeO	9·44(17)	10·26(131)	15·22(58)	11·67(45)	10·72(29)	9·32(25)	9·47(36)	10·58(55)	9·83(36)	7·81(23)	9·56(38)
MnO	0·37(3)	0·44(2)	0·47(5)	0·44(5)	0·41(3)	0·35(3)	0·40(5)	0·33(3)	0·28(4)	0·25(1)	0·28(3)
MgO	15·37(13)	14·27(36)	11·20(23)	13·09(56)	14·12(37)	15·43(19)	14·99(68)	13·75(45)	14·31(33)	14·80(30)	14·31(34)
CaO	10·56(7)	11·13(40)	8·90(25)	10·30(22)	10·57(14)	10·88(15)	10·61(52)	11·20(17)	11·41(15)	11·72(11)	11·52(14)
Na_2O	2·67(6)	2·63(6)	2·69(6)	2·59(8)	2·64(8)	2·57(6)	2·57(4)	2·51(8)	2·49(7)	2·52(5)	2·50(6)
K_2O	0·65(2)	0·67(3)	0·58(3)	0·67(5)	0·66(3)	0·71(4)	0·64(6)	0·58(6)	0·62(5)	0·71(3)	0·64(4)
Total	96·37(33)	95·46(40)	97·00(61)	96·24(21)	96·46(59)	96·18(57)	96·12(70)	96·70(61)	96·45(41)	95·90(43)	96·24(83)
Mg#	75(1)	71(4)	57(2)	67(4)	70(3)	75(2)	74(5)	70(4)	72(3)	77(2)	73(3)
$K_D^{Fe–Mg}$	0·35(3)	0·43(7)	0·36(3)	0·40(3)	0·37(2)	0·30(8)	0·47(4)	0·35(2)	0·33(2)	0·29(2)	0·34(2)
PS (μm)	13	9	6	6	13	13	6	13*	19	19	19
Nb	37(1)	57(4)	103(14)	70(1)	50 (7)	26(3)	51 (8)	97(5)	61(6)	57 (10)	52 (12)
Ta	26(2)	37(6)	81(10)	46(4)	35(2)	20 (1)	43(6)	77(3)	58 (7)	50(13)	49(19)
Cs	0·61(43)	0·21(8)	1·30(135)	0·73(88)	0·00(0)	0·30(14)	1·13(18)	0·87(13)	0·30(5)	0·33(3)	0·28(3)
Nb/Ta	1·41(11)	1·54(27)	1·27(23)	1·50(28)	1·45(21)	1·26(15)	1·21(25)	1·26(9)	1·05(16)	1·15(38)	1·07(50)
D_{Nb}	0·24(2)	0·36(2)	0·70(10)	0·42(7)	0·31(4)	0·16(2)	0·33(5)	0·67(4)	0·41(4)	0·41(7)	0·36(9)
D_{Ta}	0·23(3)	0·30(5)	0·64(8)	0·35(3)	0·29(2)	0·17(1)	0·37(6)	0·68(3)	0·51(6)	0·45(13)	0·44(18)
D_{Nb}/D_{Ta}	1·04(14)	1·21(22)	1·20(20)	1·19(23)	1·06(15)	0·93(11)	0·89(20)	0·99(8)	0·81(13)	0·91(30)	0·82(39)
D_{Ti}	2·36(19)	3·53(78)	5·67(52)	3·92(25)	3·18(25)	2·26(15)	8·69(105)	3·07(36)	2·42(21)	2·43(13)	2·31(27)

*Only one analysis was obtained and the counting errors of LA-ICP-MS are used.

Nb, Ta and Ti partition coefficients were calculated with data from this table and Table 4, major element oxides in wt % by EMPA ($n = 6$–12), Nb, Ta and Cs in ppm by LA-ICP-MS ($n = 3$–7). PS, n.a., numbers in parenthesis and Mg# as in Table 4. $K_D^{Fe–Mg}$, mineral/melt Fe–Mg exchange distribution coefficients $K_D^{Fe–Mg} = (X_{Fe}^{amp}/X_{Mg}^{amp})(X_{Mg}^{lid}/X_{Fe}^{lid})$. Standard deviation of A/B (A = Nb or D_{Nb}; B = Ta or D_{Ta}) was calculated by $SD_{A/B} = (SD_A{}^2/B^2 + A^2 \times SD_B{}^2/B^4)^{0.5}$. Standard deviation of $K_D^{Fe–Mg}$ was calculated by $SD_{KD} = \{[(SD_{Fe}{}^{amp} \times C_{Mg}{}^{lid})^2 + (C_{Fe}{}^{amp} \times SD_{Mg}{}^{lid})^2]/(C_{Mg}{}^{amp} \times C_{Fe}{}^{lid})^2 + (C_{Fe}{}^{amp} \times C_{Mg}{}^{lid})^2 \times [(SD_{Mg}{}^{amp} \times C_{Fe}{}^{lid})^2 + (C_{Mg}{}^{amp} \times SD_{Fe}{}^{lid})^2]/(C_{Mg}{}^{amp} \times C_{Fe}{}^{lid})^4\}^{0.5}$.

Amphibole composition

Amphibole in single samples is compositionally homogeneous (Table 5). All have 40–43 wt % SiO_2, 12–15 wt % Al_2O_3, 9–12 wt % CaO and 2·0–2·8 wt % Na_2O, with Mg#, TiO_2 and K_2O varying with bulk composition and experimental conditions. Amphibole–melt Fe–Mg exchange distribution coefficients $[K_D^{Fe-Mg} = (X_{Fe}^{amp}/X_{Mg}^{amp})\ (X_{Mg}^{lid}/X_{Fe}^{lid})]$ range from 0·27 to 0·47 (Table 5) with an average of 0·34 ± 0·06. The nearly constant K_D value indicates that equilibrium has been approached for the crystallization of amphiboles in this study and that there is no significant amount of Fe^{3+} incorporated into the amphiboles. The Fe^{3+} content of amphibole (minimum, maximum and mean in Supplementary Data Table S2) was estimated from the ideal crystal chemistry of the sum of cations (Na + K + Ca) = 13, and the minimum value was used to calculate the unit formula of amphibole. Based on the general formula $A_{0-1}B_2C_5T_8O_{22}(OH)_2$ of amphibole (Leake *et al.*, 1997) and the cation site assignments (^{XII}A: K^+, Na^+; ^{VIII}B (M4): Na^+, Ca^{2+}, Mn^{2+}, Fe^{2+}, Mg^{2+}; ^{VI}C (M1, 2, 3): Ti^{4+}, Al^{3+}, Fe^{3+}, Cr^{3+}, Mn^{2+}, Fe^{2+}, Mg^{2+}; ^{IV}T: Si^{4+}, Al^{3+}), nearly all the amphiboles are calcic amphiboles with Ca^{2+} in the M4 site ranging from 1·40 to 1·84 (Supplementary Data Table S2). These amphiboles can be generally classified as pargasite or a solid-solution of pargasite and magnesio-hastingsite.

Amphiboles crystallized from the MKB compositions have <2·0 wt % TiO_2 and 0·32–0·55 wt % K_2O, but those crystallized from the XT168N composition are generally higher in TiO_2 (1·5–3·5 wt %) and K_2O (0·58–0·71 wt %), indicating that the TiO_2 and K_2O contents of amphibole reflect the bulk compositions (Table 1). The Mg# values of amphiboles from the MKB experiments range from 46 to 75, whereas those from the XT168N experiments range from 57 to 77 (Table 5). Amphibole Mg# is to a large extent related to the amount of crystallization. Because both lower temperature and lower H_2O content lead to more amphibole crystallization, amphibole Mg# will decrease at low temperatures or low melt H_2O contents. The decrease of amphibole Mg# with decreasing melt H_2O content is well indicated by the multi-capsule experiments (Fig. 7), whereas its decrease with decreasing temperature is indicated by the two samples (NT33 and NT35) in which both the run temperature (850°C) and amphibole Mg# (46) are the lowest in this study.

Amphibole/melt Nb, Ta and Ti partition coefficients

Nb, Ta and Ti partition coefficients between amphibole and melt for the mid-K (MKB) and high-K (XT168N) systems are in the range of 0·16–0·90 for D_{Nb}, 0·13–0·68 for D_{Ta}, 1·81–10·61 for D_{Ti} and 0·76–2·81 for D_{Nb}/D_{Ta} (Table 5). These data are plotted in Fig. 8 together with published data for basanites and alkali basalts (Supplementary Data Table S1-1). In comparison, D_{Nb}, D_{Ta}, D_{Ti} and D_{Nb}/D_{Ta} from our mid-K and high-K systems overlap the published data for basanites and alkali basalts, although our data are generally at the high end of all the data, especially for D_{Ti} values. Taken together, the data show that D_{Nb}, D_{Ta} and D_{Nb}/D_{Ta} are correlated with D_{Ti}. In general, each of them increases with D_{Ti} (Fig. 8a–c), and when D_{Ti} is lower than 2·0–3·0, the increase of D_{Nb} and D_{Ta} with D_{Ti} is pronounced, whereas when D_{Ti} is higher than ~3·0, their increase with D_{Ti} gradually decreases. In both cases, the increase of D_{Nb} with D_{Ti} is generally more significant than that of D_{Ta} with D_{Ti}, leading to an increase of D_{Nb}/D_{Ta} with D_{Nb} (Fig. 8d). The variations of D_{Nb}, D_{Ta}, D_{Ti} and D_{Nb}/D_{Ta} are dependent on the experimental and compositional conditions. The wide range of experimental conditions (P, T, H_2O, fO_2) and compositional variations (bulk TiO_2 and K_2O, amphibole Mg# and melt X_{nf}/X) in this study and in the literature allow us to constrain the main factors that affect the Nb, Ta and Ti partitioning.

Bulk TiO_2 and K_2O show no effects on the partitioning. As shown by one group of multi-capsule experiments with bulk TiO_2 varying from 0·0 to 0·3, 0·6 and 1·2 wt % (Fig. 9a), D_{Nb}, D_{Ti} and D_{Nb}/D_{Ta} are invariable within analytical error, although TiO_2 in amphibole linearly increases with increasing bulk TiO_2. This indicates that the TiO_2 contents in the bulk composition and in amphibole do not affect the Nb, Ta and Ti partitioning, and thus the correlation of D_{Nb}, D_{Ta} and D_{Nb}/D_{Ta} with D_{Ti} mentioned above indicates only that the behavior of Nb and Ta is similar to that of Ti. This also indicates that Ti partitioning obeys Henry's Law and that the Nb, Ta and Ti partitioning reached equilibrium.

D_{Nb}, D_{Nb}/D_{Ta} and D_{Ti} have no clear variations with amphibole K_2O under similar P–T conditions (Fig. 9b), although K_2O in amphibole obviously increases from the MKB and XT168N systems to the basanites and alkali basalts (Supplementary Data Table S1-2). This indicates that the K_2O content in amphibole has no effect on the Nb, Ta and Ti partitioning. Because the K_2O content in amphibole reflects the K_2O content in the bulk composition, bulk K_2O should also have no effect on the partitioning. However, this does not necessarily mean that the bulk composition has no effect on the partitioning. At the given P–T–H_2O conditions, different bulk compositions are expected to have different amphibole Mg# and melt compositions and thus the bulk composition must have an effect on the partitioning, but such an effect is achieved via its influence on amphibole Mg# and melt composition.

Oxygen fugacity also shows no effect on the partitioning. NT48 (no fO_2 buffer) and NT50 (graphite-buffered fO_2) are two samples with a large fO_2 difference (FMQ + 0·86 vs FMQ – 6·1; Fig. 9c). Both samples were run at the same P and T conditions, and their amphibole Mg#, melt composition (X_{nf}/X) and melt H_2O content are also similar. However, their amphibole/melt D_{Nb}, D_{Ti} and D_{Nb}/D_{Ta} show no substantial difference, indicating that fO_2 has no effect on the partitioning. It should be noted that the lack of observable effect of fO_2 on the Nb, Ta and Ti partitioning is consistent with previous results reported by Dalpé & Baker (2000) and Adam *et al.*

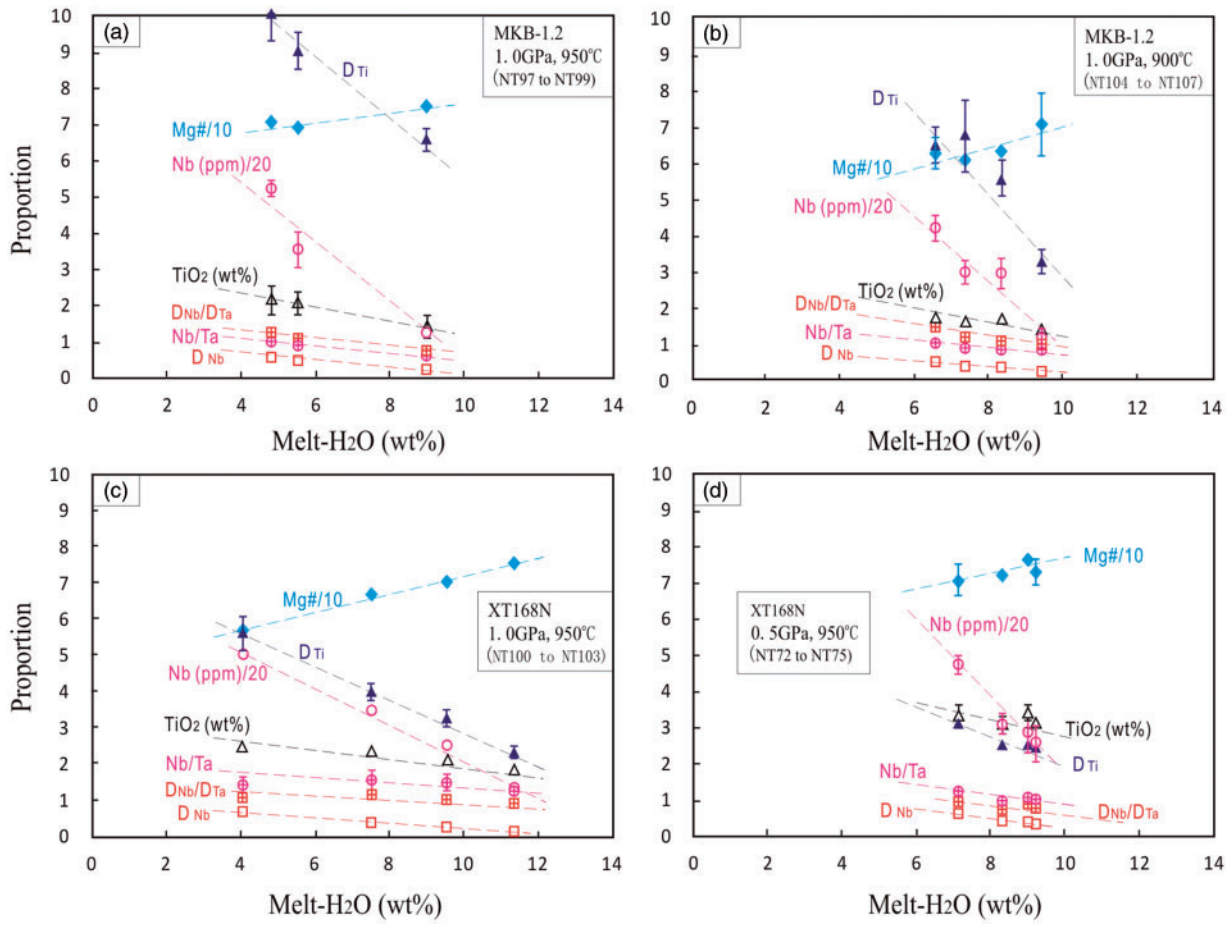

Fig. 7. Variations of Mg#, Nb and Nb/Ta in amphibole and D_{Nb}, D_{Ti} and D_{Nb}/D_{Ta} for amphibole/melt with melt H_2O content in the multi-capsule experiments. Data from Table 5. Error bars are not shown when they are smaller than the symbol.

(2007). This suggests that (1) the oxidation states of Nb, Ta and Ti are invariable in our experimental conditions, and (2) the variation of Fe^{2+}/Fe^{3+} in amphibole in response to the change of fO_2 does not significantly change its crystal structure.

It is difficult to separate thoroughly the effects of *P*, *T*, H_2O, amphibole Mg# and melt X_{nf}/X on the Nb, Ta and Ti partitioning because amphibole Mg#, melt X_{nf}/X and melt H_2O always varied with the degree of crystallinity, which is *T*, *P* and H_2O dependent. To separate the effects of variables as much as possible, we screened the data from this study and the literature to allow the examination of variables associated with large changes in the above parameters.

The data (Supplementary Data Table S1-3) that were used to examine the effect of pressure (0·5–1·5 GPa) are those for temperatures at 950–1050°C and melt H_2O at 6·0–10 wt %. D_{Ti} and D_{Nb} generally decrease, as shown in Fig. 10, but D_{Nb}/D_{Ta} does not vary with increasing pressure. This indicates that pressure results in a simultaneous decrease of D_{Nb} and D_{Ta} and thus it does not significantly affect D_{Nb}/D_{Ta}. These results are similar to the observations of Adam & Green (2003). Our D_{Ti}, D_{Nb} and D_{Nb}/D_{Ta} values are generally higher than the published data for basanites and alkali basalts, as shown in Fig. 10. This is due to the small differences of temperature and melt X_{nf}/X.

The data (Supplementary Data Table S1-4) that were used to examine the effects of *T* (850–1100°C) and melt X_{nf}/X (0·4–0·8) are those obtained at $P = 1·0–1·5$ GPa and melt $H_2O = 6·0–10$ wt %, whereas the data (Supplementary Data Table S1-5) that were used to clarify the effect of amphibole Mg# (60–100) are those with the same ranges of *P* and melt H_2O but the temperature range was reduced to 950–1050°C. To examine the effect of melt H_2O content (1·5–14·0 wt %), we used the data (Supplementary Data Table S1-6) at $P = 1·0–1·5$ GPa and $T = 950–1050$°C. From these datasets, two important points can be observed: (1) D_{Ti}, D_{Nb} and D_{Nb}/D_{Ta} decrease with increasing temperature (Fig. 11, a1–a3), amphibole Mg# (Fig. 11, c1–c3) and melt H_2O content (Fig. 12a–c), but increase with increasing melt X_{nf}/X or melt polymerization (Fig. 11, b1–b3); (2) at a given value of the examined variable, D_{Ti}, D_{Nb} and D_{Nb}/D_{Ta} values for the MKB and XT168N basalts are generally higher than the published values for basanites and alkali basalts. It should be noted that our experiments were conducted at lower

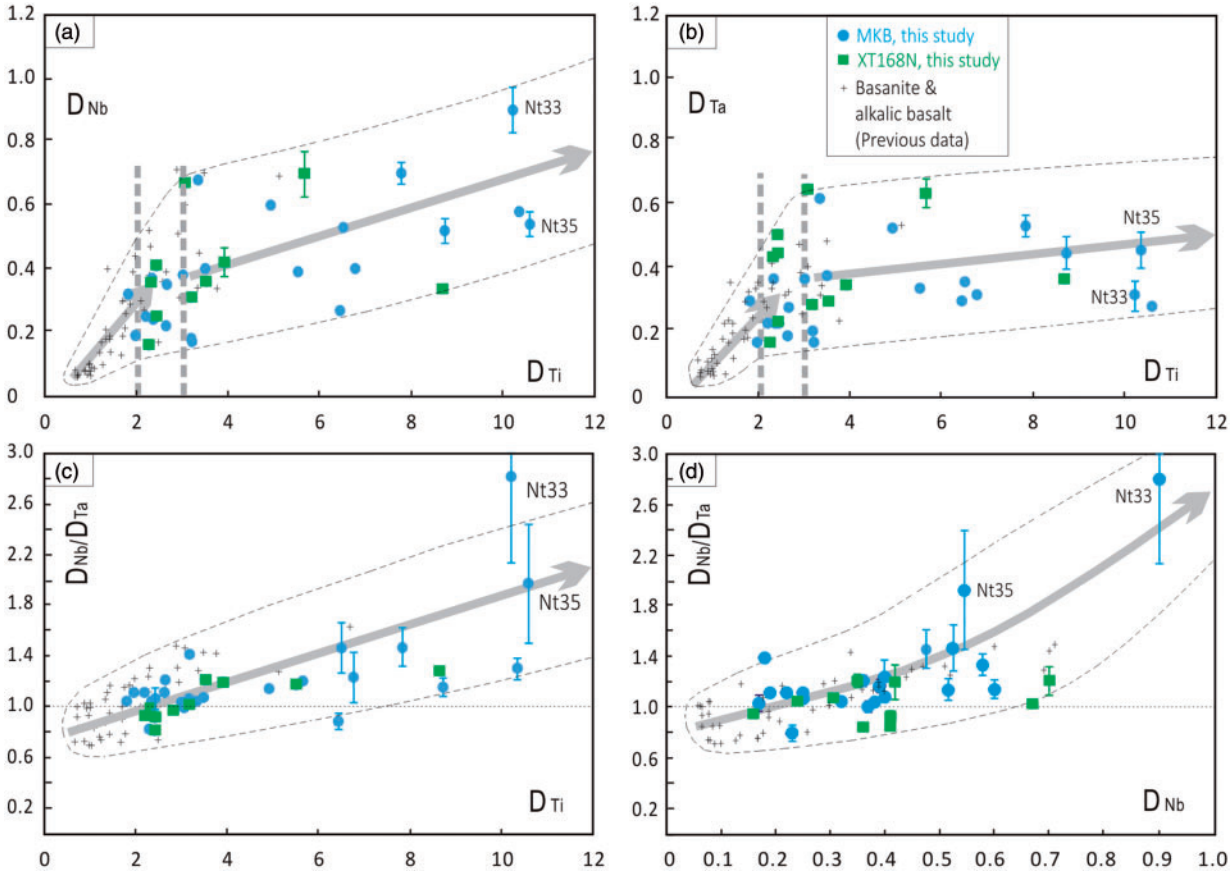

Fig. 8. D_{Nb} vs D_{Ti} (a), D_{Ta} vs D_{Ti} (b), D_{Nb}/D_{Ta} vs D_{Ti} (c) and D_{Nb}/D_{Ta} vs D_{Nb} (d) for amphibole/melt in the mid-K (MKB) and high-K (XT168N) basaltic systems. Published data for basanites and alkali basalts are shown for comparison; data of this study are from Table 5 and published data (Supplementary Data Table S1-1) for basanites and alkali basalts are from Adam *et al.* (1993, 2007), Dalpé & Baker (2000), Tiepolo *et al.* (2000) and Adam & Green (2003, 2006).

temperatures (≤1010°C) than previous experiments (generally > 1000°C) and thus have slightly higher melt X_{nf}/X values.

Two experiments (NT33 and NT35) with ~4·5 wt % initial H_2O conducted at 850°C (the lowest run temperature in this study) show the highest amphibole/melt D_{Ti} and D_{Nb}/D_{Ta} values (Fig. 8), the lowest amphibole Mg# (Table 5) and the highest melt X_{nf}/X values (Table 4). These indicate that at a given initial H_2O condition, these D values will significantly increase with the variations in temperature and compositions of amphibole and melt during crystallization induced by cooling. D_{Ti}, D_{Nb} and D_{Nb}/D_{Ta} variations with amphibole Mg# and melt X_{nf}/X were previously reported by Tiepolo *et al.* (2000, 2007), whereas the variation of these values with T and H_2O are new findings of this study. In the four groups of multi-capsule experiments (Fig. 7), Nb and Nb/Ta in amphibole and D_{Ti}, D_{Nb} and D_{Nb}/D_{Ta} between amphibole and melt increase with decreasing melt H_2O content, clearly indicating a significant effect of melt H_2O content, although some contributions from the effects of amphibole Mg# and/or melt X_{nf}/X (both of them vary with melt H_2O content and crystalline degree) cannot be excluded. Xiong *et al.* (2011) observed that rutile/melt D_{Nb} and D_{Nb}/D_{Ta} increase with decreasing melt H_2O content and temperature (Fig. 12d). These variations were attributed to the effects of both T and H_2O on the compatibility of Nb and Ta in the melt, specifically, the activity coefficients and/or speciation of Nb and Ta in the melt. These observations are convincing because only T and melt H_2O are the variables in their experiments (rutile is a single-component phase—TiO_2 and melt composition and pressure were fixed). Given that both T and H_2O have pronounced effects on the compatibility of Nb and Ta in the melt, the two factors must also influence amphibole/melt Nb and Ta partitioning.

The effects of T and H_2O on amphibole/melt Nb, Ta and Ti partitioning are important findings. In this study, high D_{Ti} (>3·0), D_{Nb} (>0·4) and D_{Nb}/D_{Ta} (>1·2) values are generally from the experiments with low temperatures (≤900°C, such as NT33 and NT35) or low melt H_2O contents (<6·0 wt %, such as NT97 and NT104). This is also true for the experiments on basanites and alkali basalts: the experiments of Tiepolo *et al.* (2000) give generally higher D_{Ti}, D_{Nb} and D_{Nb}/D_{Ta} values than other experiments (Adam *et al.*, 1993, 2007; Dalpé & Baker, 2000; Adam & Green, 2003, 2006) (Fig. 2 and Supplementary

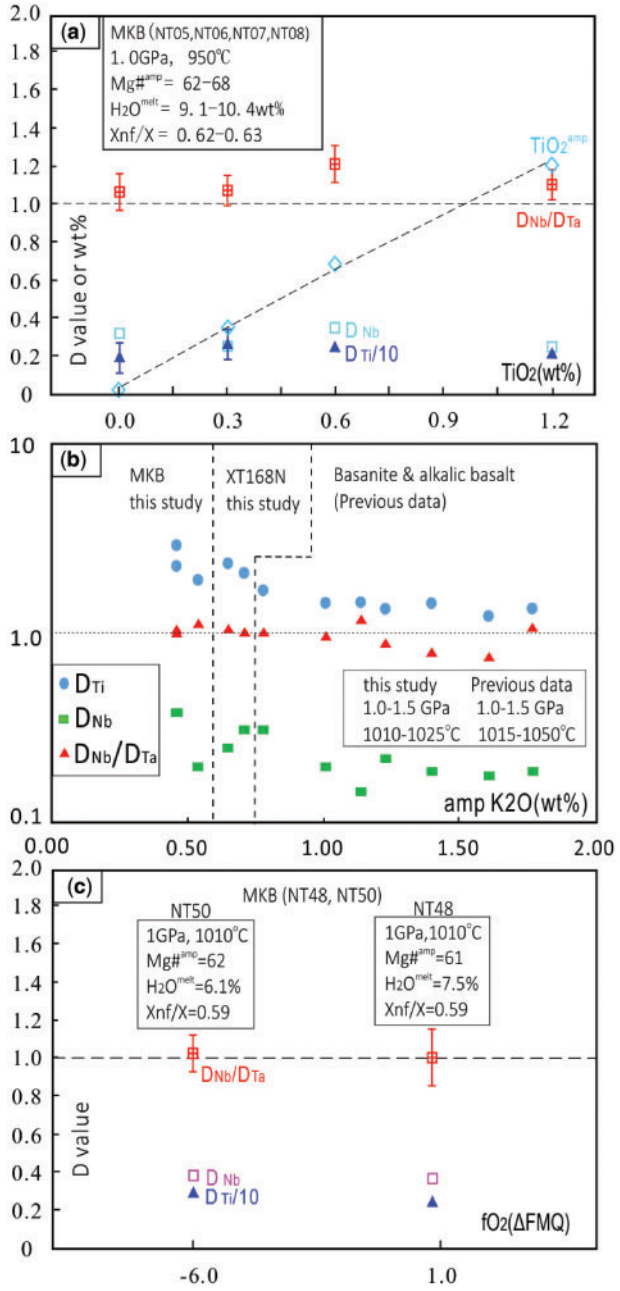

Fig. 9. D_{Ti}, D_{Nb} and D_{Nb}/D_{Ta} vs bulk TiO_2 (a), amphibole K_2O (b) and fO_2 (c), showing no correlation between the D values (D_{Ti}, D_{Nb} and D_{Nb}/D_{Ta}) and these variables. Data in (a) and (c) are from Table 5, and data in (b) are from Supplementary Data Table S1-2.

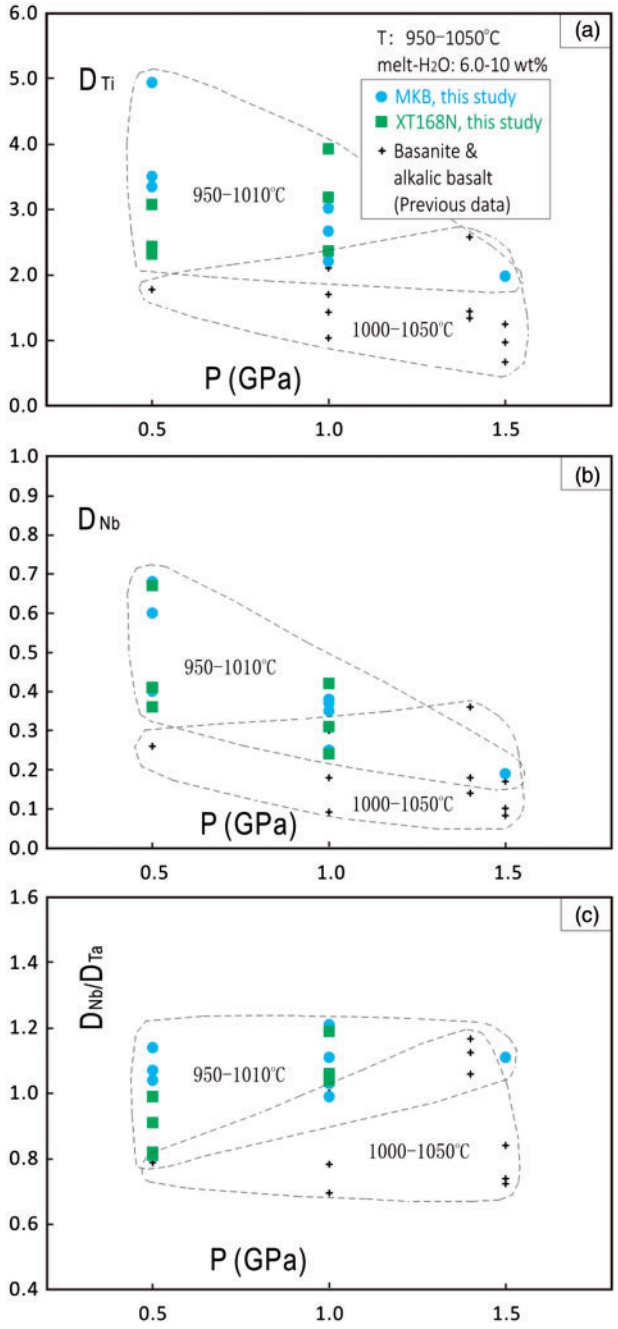

Fig. 10. Variations of amphibole/melt D_{Ti}, D_{Nb} and D_{Nb}/D_{Ta} with pressure, showing that D_{Ti} and D_{Nb} generally decrease but D_{Nb}/D_{Ta} does not change with increasing pressure. Data from Table 5 and Supplementary Data Tables S1-3 and S1-4.

Data Table S1-1) because the former were conducted mostly at lower melt H_2O contents or lower temperatures than the latter.

Compositions and Nb and Ta partition coefficients for other minerals

Olivine compositions (Supplementary Data Table S3, $n=6$) range from Fo_{70} to Fo_{76}. The olivine–melt Fe/Mg K_D is $0{\cdot}31 \pm 0{\cdot}01$, close to the literature value of $0{\cdot}33 \pm 0{\cdot}01$ (Gaetani & Grove, 1998). Orthopyroxenes ($Wo_{2{\cdot}4–4{\cdot}2}En_{61{\cdot}1–76{\cdot}8}Fs_{20{\cdot}9–35{\cdot}4}$, $n=7$) have Mg# = 64–79 and contain ~5·0 wt % Al_2O_3, <0·3 wt % TiO_2 and <2·0 wt % CaO. The opx–melt Fe/Mg K_D is $0{\cdot}27 \pm 0{\cdot}03$, slightly lower than the literature value of $0{\cdot}31 \pm 0{\cdot}02$ (Falloon & Danyushevsky, 2000). Clinopyroxenes ($Wo_{37{\cdot}6–47{\cdot}9}En_{31{\cdot}8–41{\cdot}9}Fs_{12{\cdot}5–22{\cdot}7}$, $n=10$) are Ca-rich (17–22·5 wt % CaO). They have Mg# = 60–76 and 4·8–9·0 wt % Al_2O_3, <0·70 wt % TiO_2 and 0·3–1·4 wt % Na_2O. The cpx–melt Fe/Mg K_D is $0{\cdot}31 \pm 0{\cdot}07$, close to the literature value of $0{\cdot}33 \pm 0{\cdot}02$ (Gaetani & Grove,

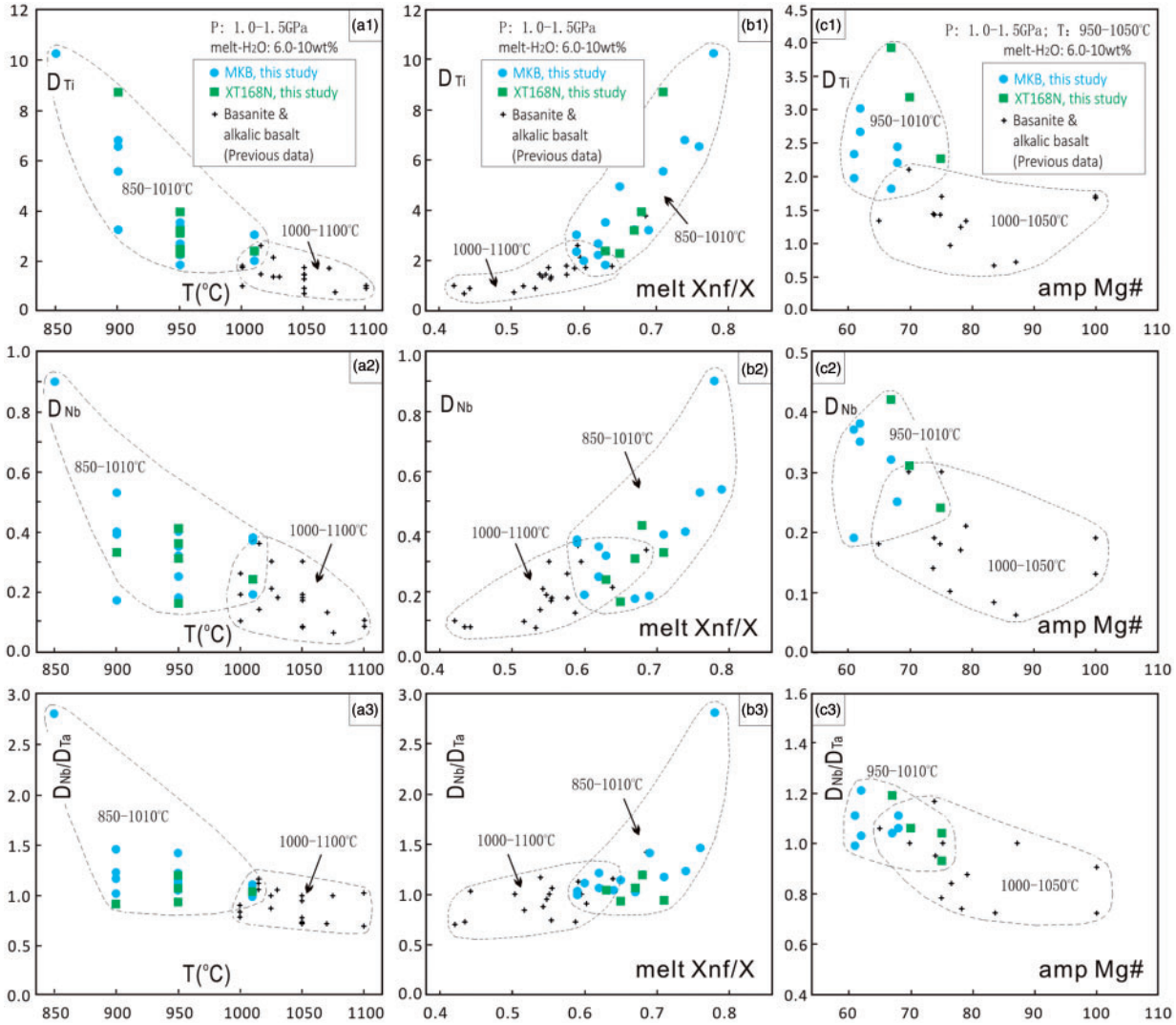

Fig. 11. Variations of amphibole/melt D_{Ti}, D_{Nb} and D_{Nb}/D_{Ta} with temperature (a1–a3), melt X_{nf}/X (b1–b3) and amphibole Mg# (c1–c3), showing that D_{Ti}, D_{Nb} and D_{Nb}/D_{Ta} increase with decreasing temperature and amphibole Mg#, but increase with increasing melt X_{nf}/X. Data from Table 5 and Supplementary Data Tables S1-3 and S1-4.

1998). Garnets in the rims ($al_{43–53}py_{23–35}gr_{20–22}an_{0·2–2}$, $n = 3$) are Fe-rich (21·2–27·8 wt % FeO) with Mg# = 29–45. They contain ~20·5 wt % Al_2O_3, 6·1–9·5 wt % MgO and 8·3–9·0 wt % CaO. The garnet–melt Fe/Mg K_D is 0·76 ± 0·04. Nb and Ta partition coefficients for olivine–, opx–, cpx– and garnet–melt (one pair each mineral) were obtained from four samples in the MKB experiments (Supplementary Data Table S3). The results show that D_{Nb} and D_{Ta} for these mafic minerals are generally <0·01, consistent with previous results (Adam & Green, 2006) and suggesting that these minerals have negligible influence on the fractionation of Nb/Ta during magmatic evolution. Plagioclases have compositions of $An_{48·5–80·6}Ab_{18·9–50·2}Or_{0·3–3·1}$ ($n = 9$). No Nb and Ta partition coefficients for this phase were obtained.

Oxides produced in this study are spinel group solid solutions composed of Al_2O_3, Fe_2O_3, FeO, MgO, TiO_2 and Cr_2O_3. Their compositions and cations per formula unit calculated assuming the perfect stoichiometry (AB_2O_4, A = Mg, Fe^{2+}; B = Al, Fe^{3+}, Ti, Cr), are given in Supplementary Data Table S4. Based on the Fe, Ti and Cr contents, they can be generally divided into three populations: magnetite, Ti-magnetite and Cr-spinel. Magnetite is the most common oxide. Sixteen samples in the MKB experiments and seven samples in the XT168N experiments contain magnetite. Magnetite compositions from both sets of experiments overlap. They are mainly composed of FeO (FeO_t 68·76–82·68 wt %), Al_2O_3 (2·92–10·49 wt %) and MgO (1·63–7·54 wt %), with both TiO_2 and Cr_2O_3 generally less than 2·0 wt %. Thus their compositions plot mainly along the join $FeFe_2O_4$–$MgAl_2O_4$ (magnetite–spinel). Ti-magnetites were present in four MKB experiments and two XT168N experiments. They are TiO_2- and FeO_t-rich (TiO_2 8·59–15·61 wt %; FeO_t 65·81–78 wt %), and contain 1·12–7·89 wt % Al_2O_3, 1·45–8·64 wt % MgO and <2·0 wt % Cr_2O_3. The Fe- and Ti-rich characteristics indicate that they are the solid-solution along the $FeFe_2O_4$–Fe_2TiO_4 (magnetite–ulvöspinel) join. Cr-spinels were present in four MKB experiments and three XT168N experiments.

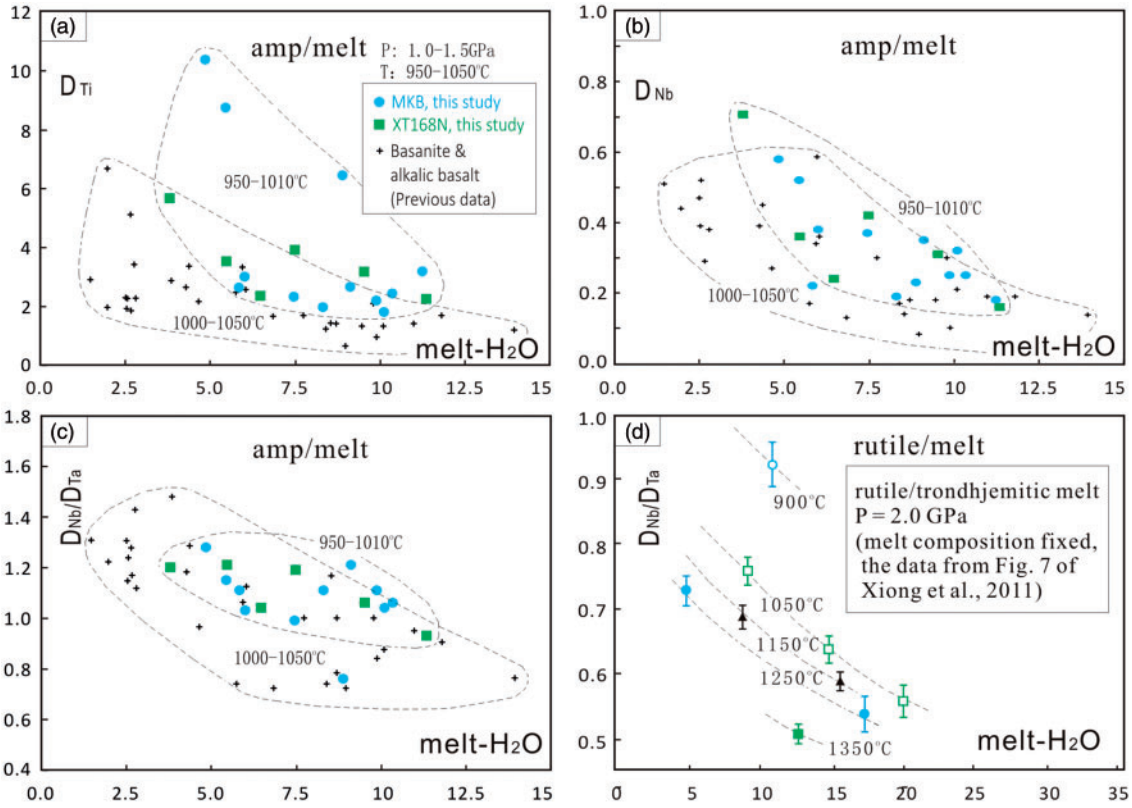

Fig. 12. D_{Ti} (a), D_{Nb} (b) and D_{Nb}/D_{Ta} (c) vs melt H_2O content for amphibole/melt at 1·0–1·5 GPa and 950–1050°C and D_{Nb}/D_{Ta} vs melt H_2O for rutile/melt (d) at 2·0 GPa and 900–1350°C, showing significant effects of melt H_2O and temperature on the Nb, Ta and Ti partitioning. Data for amphibole–melt pairs from Table 5 and Supplementary Data Table S1-5, and for rutile–melt pairs from Xiong *et al.* (2011).

They have high contents of Cr_2O_3 (11·07–25·56 wt %), FeO_t (34·97–74·25 wt %) and Al_2O_3 (6·72–47·09 wt %), and some MgO (1·50–9·66 wt %) and minor TiO_2 (mostly < 2·0 wt %). Thus they plot mainly in the $FeCr_2O_4$–$FeFe_2O_4$–$MgAl_2O_4$ (chromite–magnetite–spinel) triangle.

Nb and Ta partition coefficients for oxide–melt were obtained in four experiments: one pair for magnetite–melt and the other three pairs for Ti-magnetite–melt (Supplementary Data Table S4). The magnetite–melt D_{Nb} and D_{Ta} are 0·032 and $D_{Ta} = 0·06$, respectively, with $D_{Nb}/D_{Ta} = 0·52$. This is approximately in agreement with the low magnetite–melt D values [average ($n = 6$) $D_{Nb} = 0·10$, $D_{Ta} = 0·12$ and $D_{Nb}/D_{Ta} = 0·83$] in the hydrous magma systems of Nielsen & Beard (2000). The Ti-magnetite–melt Nb and Ta D values (three pairs) are in the range: $D_{Nb} = 0·35$–$2·12$, $D_{Ta} = 0·54$–$2·78$ and $D_{Nb}/D_{Ta} = 0·66$–$0·76$. For the Cr-spinels, EMPA showed that Nb_2O_5 and Ta_2O_5 contents in this phase are lower than their detection limits of 0·01 wt %, indicating low D_{Nb} and D_{Ta} for this phase. Therefore, magnetite and Cr-spinel would have negligible effect on fractionation of Nb/Ta. Only Ti-magnetite may have a substantial contribution to Nb/Ta fractionation. $D_{Nb}/D_{Ta} < 1·0$ for Ti-magnetite suggests that this phase will result in higher Nb/Ta in the coexisting melt.

DISCUSSION

Mechanisms causing amphibole–melt D_{Nb}/D_{Ta} fractionation

For the site occupancy in calcic amphiboles, Robinson *et al.* (1982) suggested that Nb and Ta may favor the M2 site owing to their behavior being similar to that of Ti. However, the single-crystal structure refinement results of Tiepolo *et al.* (2000) indicate that Ti mainly occupies the M1 site and amphibole–melt D_{Nb} has a strongly positive correlation with $^{M1}D_{Ti}$ but only a weakly positive correlation with $^{M2}D_{Ti}$. Tiepolo *et al.* (2000) thus suggested that Nb and Ta, following Ti, are mainly ordered on the M1 site owing to dehydrogenation at the O3 site (substitution of OH^- by O^{2-}), which is coupled by the substitution of Mg^{2+} and Fe^{2+} by the highly charged cations Ti, Nb and Ta in balancing the presence of the oxy-component.

Based on a XANES spectra study (Burnham *et al.*, 2012), both Nb and Ta in silicate melts are exclusively present as Nb^{5+} and Ta^{5+} under conditions of P, T and fO_2 in the crust and upper mantle, and they are expected to be incorporated into mineral crystals also as Nb^{5+} and Ta^{5+}. As two same valence-state cations, Nb and Ta partitioning between mineral and melt is mainly dependent on their ionic radii and the compositions (or structures)

of both crystal and melt, which are dependent upon the experimental conditions (*P*, *T* and melt H_2O). The high variability of amphibole–melt D_{Nb}/D_{Ta} (0·76–2·81) implies that these factors affect the M1 site size and the extent of dehydrogenation in amphibole, and the activity coefficients and/or speciation of Nb and Ta in the melt.

Amphibole–melt D_{Nb} and D_{Nb}/D_{Ta} are strong inverse functions of amphibole Mg#, which correlates well with the dehydrogenation (Tiepolo *et al.*, 2000). Tiepolo *et al.* (2000) found that D_{Nb}/D_{Ta} increases with the M1 site size and thus inferred that the ionic radius of Nb is 0·01–0·02 Å larger than that of Ta ($r^{Nb} \sim 0{\cdot}66$ Å, $r^{Ta} = 0{\cdot}64$ Å). They further inferred, based on elastic-strain theory, that the inversion of D_{Nb}/D_{Ta} from $<1{\cdot}0$ to $>1{\cdot}0$ occurs if r^{Nb} and r^{Ta} lie close to the apex (r_0) of the Onuma curve. If so, we can further infer that r_0 at the M1 site will increase with decreasing Mg# because D_{Nb} and D_{Nb}/D_{Ta} strongly increase with decreasing Mg#. The inversion of D_{Nb}/D_{Ta} from $<1{\cdot}0$ to $>1{\cdot}0$ can be easily explained by the variation of r_0 at the M1 site with Mg# (Fig. 13). At a high amphibole Mg#, both r^{Nb} and r^{Ta} lie to the right of the apex of the Onuma curve (both r^{Nb} and r^{Ta} are slightly larger than r_0) and the Nb^{5+} radius is slightly larger than the Ta^{5+} radius, leading to $D_{Nb}/D_{Ta} < 1{\cdot}0$. With the decline of amphibole Mg#, r_0 at the M1 site also increases, leading to r^{Nb} lying to the left of the apex of the Onuma curve, whereas r^{Ta} still lies to the right. In this case, D_{Nb} should be close to D_{Ta} ($D_{Nb}/D_{Ta} \approx 1{\cdot}0$). At a low amphibole Mg#, both r^{Nb} and r^{Ta} are smaller than r_0; that is, both r^{Nb} and r^{Ta} lie in the left of the apex of Onuma curve. In this case, D_{Nb}/D_{Ta} must be $>1{\cdot}0$ because r^{Nb} is situated closer to r_0 than is r^{Ta}.

Temperature, melt composition and melt H_2O content also have strong effects on the Nb/Ta fractionation.

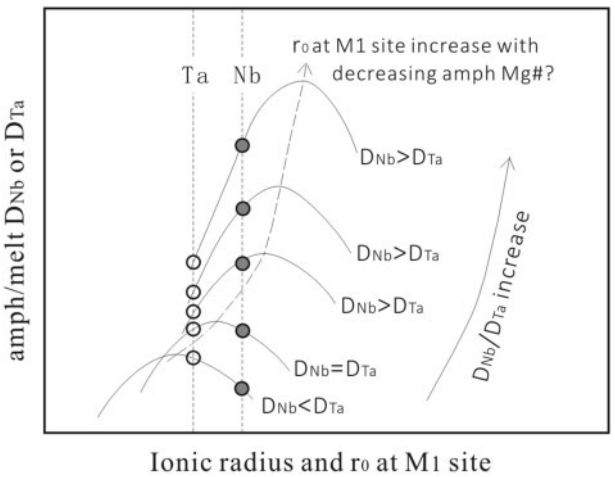

Fig. 13. The schematic dependence of amphibole/melt D_{Nb} and D_{Ta} on the site dimension, showing that D_{Nb}, D_{Ta} and D_{Nb}/D_{Ta} increase with the M1 site size (r_0) and that an inversion of D_{Nb}/D_{Ta} from $<1{\cdot}0$ to $>1{\cdot}0$ will occur assuming the ionic radius of Nb is larger than that of Ta and Nb and Ta lie close to the Onuma curve apex (Tiepolo *et al.*, 2000). The M1 site size (r_0) increases with decreasing amphibole Mg#, which is dehydrogenation dependent on the O3 site (substitution of OH^- by O^{2-}).

Amphibole/melt D_{Nb} and D_{Nb}/D_{Ta} increase with decreasing temperature and melt H_2O content and increasing melt polymerization, probably owing to the different effects of these parameters on the activity coefficients of Nb and Ta in the melt (Linnen & Keppler, 1997). In addition, H_2O may also strongly influence the speciation of Nb over that of Ta in the melt, which is expected to cause a large difference between the compatibilities of Nb and Ta in the amphibole structure. Adam *et al.* (2014) observed a distinct fractionation of Nb from Ta (with the vapor having higher Nb/Ta) in the melt–fluid coexisting system. A recent study (Timofeev *et al.*, 2015) demonstrated that Nb_2O_5 (solid) can be dissolved into aqueous fluids primarily as the species $Nb(OH)_4^+$, whereas Ta_2O_5 is still relatively insoluble. We infer that in hydrous silicate melts, a significant amount of $Nb(OH)_4^+$ in addition to Nb_2O_5 clusters is also probably present, achieved by the reaction $Nb_2O_5 + 5H_2O = 2Nb(OH)_4^+ + 2(OH)^-$. With this reaction, the decrease of D_{Nb}/D_{Ta} with melt H_2O content can also be explained. At a low melt H_2O content, the amount of $Nb(OH)_4^+$ in the melt is limited and thus Nb_2O_5 will significantly incorporate into amphibole, whereas at a high melt H_2O content, $Nb(OH)_4^+$ in the melt will significantly increase and thus cause a decrease of the amount of Nb incorporating into amphibole because $Nb(OH)_4^+$ could not incorporate into its structure.

Nb/Ta fractionation by amphibole during arc magma evolution

The main factors that affect the Nb, Ta and Ti partitioning between amphibole and melt are *T*, H_2O and the compositions of amphibole and melt. During cooling-induced crystallization of arc magmas at crustal pressures, amphibole Mg# decreases and melt polymerization increases, leading to a continuous increase in amphibole/melt D_{Nb}, D_{Ti} and D_{Nb}/D_{Ta}. Meanwhile, melt H_2O content increases with increasing degree of crystallization, which suppresses the increase in these *D* values. Because both amphibole Mg# and melt polymerization are functions of temperature and melt H_2O content, the trend and extent of Nb/Ta fractionation in the melt by amphibole during cooling crystallization critically depends on temperature and melt H_2O content. Only low temperatures or low H_2O contents at high temperatures lead to high *D* values. In Fig. 11, a1–a3, amphibole/melt D_{Nb}, D_{Ti} and D_{Nb}/D_{Ta} can be seen to increase with decreasing temperature. For a primitive magma with a given H_2O content, Nb/Ta in the evolved melt relative to its parent magma at the early stage of crystallization may not be fractionated owing to D_{Nb}/D_{Ta} being close to 1·0. During the middle to late stages, Nb/Ta in the melt will decrease as a result of the continuous increase of D_{Nb}/D_{Ta} from $\leq 1{\cdot}0$ to $>1{\cdot}0$ in response to the decline of temperature and the variations in amphibole Mg# and melt polymerization during crystallization. Therefore, Nb/Ta fractionation in the melt will be enhanced with cooling crystallization.

Arc magmas typically contain 2–6 wt % H_2O (Sisson & Layne, 1993). The average water content for single arcs varies from 3·2 to 4·5, with a global average of 3·9 ± 0·4 wt % H_2O (Plank *et al.*, 2013). Figure 12a–c shows that at melt H_2O contents less than 5·0–6·0 wt %, D_{Nb} and D_{Nb}/D_{Ta} are generally higher than 0·30 and 1·20, respectively. At an initial H_2O of 3·0–4·3 wt % (very close to 3·9 wt %), the average values are 0·53 for D_{Nb} and 1·27 for D_{Nb}/D_{Ta} (Table 6) at 1·0 GPa and 900–950°C. The results thus indicate that in the typical H_2O content range of arc magmas, amphibole generally has high D_{Nb} and D_{Nb}/D_{Ta} and is capable of causing a substantial decrease of Nb/Ta in the melt. With the constraint of arc magma H_2O content and the Nb/Ta fractionation trend with decreasing crystallization temperature, amphibole fractionation is expected to lower Nb/Ta in the melt during arc magma evolution in crustal roots.

It should be noted that only amphibole, biotite and Ti-rich accessory phases can fractionate Nb from Ta during arc magma evolution. TiO_2 and Nb vs SiO_2 and Nb/Ta vs SiO_2, MgO and TiO_2 for global arc magmas ($n = 9116$, from http://georoc.mpch-mainz.gwdg.de/georoc/) and their average TiO_2, Nb and Nb/Ta ratios are plotted in Fig. 14. Several points can be made: (1) TiO_2 in arc magmas generally decreases with increasing SiO_2 (Fig. 14a), indicating that Ti is compatible and that significant fractional crystallization of amphibole ± biotite and/or Ti-rich phases takes place during arc magma differentiation; (2) Nb abundances (generally from 0·5 to 100 ppm, Fig. 14b) and Nb/Ta (from 5 to 22, Fig. 14c and d) show wide ranges; especially for those magmas with low SiO_2 (<52 wt %) and high MgO (>5 wt %), Nb and Nb/Ta show considerable scatter, suggesting wide ranges of Nb and Nb/Ta in the parent magmas and the mantle wedge source; (3) despite the wide range and significant scatter, the Nb/Ta ratios of arc magmas as a whole and an average decrease with increasing SiO_2 (Fig. 14c) and decreasing MgO (Fig. 14d) and TiO_2 (Fig. 14e), indicating a general decrease of Nb/Ta during arc magma evolution. This global trend should generally be controlled by fractionation of amphibole ± biotite rather than Ti-rich phases, because the latter result in a Nb/Ta fractionation trend opposite to the global trend and the trend caused by amphibole ± biotite fractionation (Fig. 14f). Because biotite typically crystallizes from evolved, K-enriched, felsic magmas, it is suggested that amphibole is the main phase responsible for the global Nb/Ta fractionation trend. However, it should be noted that, although amphibole controls the overall trend of Nb/Ta fractionation, the wide range and significant scatter of Nb/Ta in the arc magmas indicate that the effect of Ti-rich phases on the Nb/Ta fractionation cannot be ignored. Many arc magmas contain accessory ilmenite or Ti-magnetite (Woodhead *et al.*, 1993; Caulfield *et al.*, 2008). Fractional crystallization of these Ti-rich phases could be responsible for the scatter of Nb/Ta in evolved magmas. The wide ranges in Nb and Nb/Ta for the parent arc magmas (low-SiO_2 and high-MgO endmember, Fig. 14b–d) may be attributed to the mantle source, or depletion in Nb, Ta and Nb/Ta by previous partial melting events (Caulfield *et al.*, 2008) and/or enrichment in Nb, Ta and other incompatible elements by slab-derived melts or supercritical fluids (Kessel *et al.*, 2005).

Negative Nb, Ta and Ti anomalies and Nb/Ta fractionation

It is well known that arc magmas have pronounced negative anomalies in Nb, Ta and Ti. These anomalies cannot be attributed to the presence of residual Ti-rich phases in their mantle sources because TiO_2 solubility is very high in basaltic melts and thus the stability of Ti-rich phases is impossible during mantle partial melting (Green & Pearson, 1986; Ryerson & Watson, 1987; Xiong *et al.*, 2009). These anomalies are generally ascribed to low concentrations of Nb, Ta and Ti in the mantle wedge source, combined with enrichment of other incompatible elements by slab-derived fluids or melts that are themselves depleted in Nb, Ta and Ti. However, given that amphibole/melt D_{Nb}/D_{Ta} generally increases with D_{Ti} (Fig. 8c) and $D_{Ti} > 2·0$ (up to 10) for the H_2O content range of arc magmas (Fig. 12a), it is expected that the negative Ti anomaly will be enhanced by amphibole fractionation and there should be a correlation between Ti depletion and Nb/Ta fractionation. This is indeed true. The average Nb/Ta of arc magmas generally decreases with decreasing TiO_2 (Fig. 14e). This trend is also generally controlled by amphibole ± biotite rather than by Ti-rich phases. Therefore,

Table 6: Amphibole/melt Nb and Ta partition coefficients at 1·0 GPa, 900–950°C and initial H_2O contents close to the average of 3·9 ± 0·4 wt % in arc magmas (Plank *et al.*, 2013)

Run no.	SM	Ini-H_2O (wt %)	P (GPa)	T (°C)	D_{Nb}	D_{Ta}	D_{Nb}/D_{Ta}	melt SiO_2 (wt %)	melt H_2O (wt %)	CA (wt %)	amp in CA (wt %)
NT97	MKB-1.2	4·3	1·0	950	0·58	0·46	1·28	69·47	4·85	65	52
NT104	MKB-1.2	3·3	1·0	900	0·53	0·36	1·46	71·45	6·51	70	63
NT105	MKB-1.2	4·2	1·0	900	0·40	0·32	1·23	69·62	7·35	57	74
NT100	XT168N	3·0	1·0	950	0·70	0·64	1·21	61·59	3·80	59	100
NT101	XT168N	3·7	1·0	950	0·42	0·35	1·19	61·26	7·49	49	92
					0·53 ± 0·12	0·42 ± 0·13	1·27 ± 0·11				

SM, starting material; CA, crystal assemblage (crystalline degree); amp, amphibole. Data from Tables 3, 4 and 5.

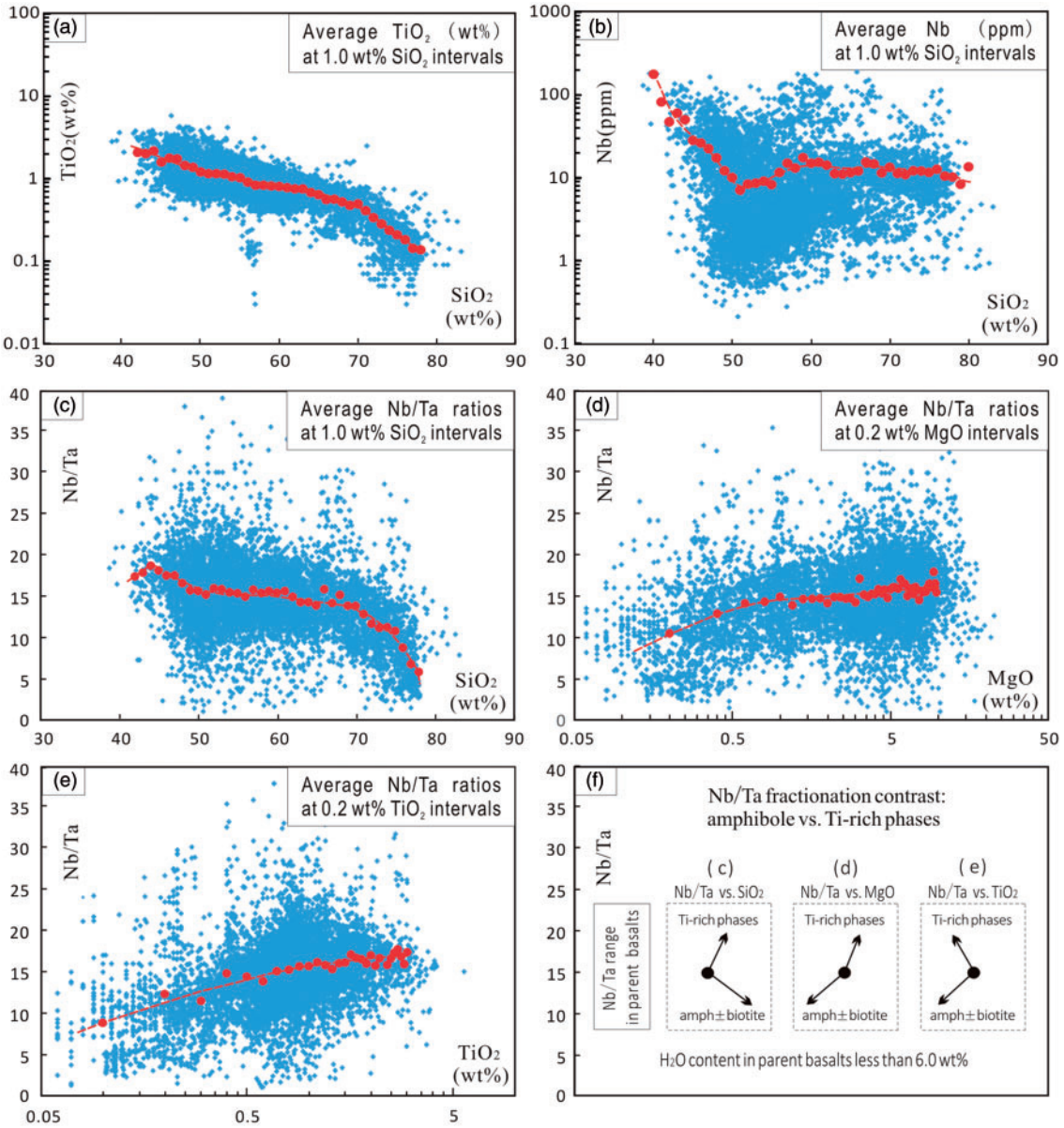

Fig. 14. TiO_2 vs SiO_2 (a), Nb vs SiO_2 (b) and Nb/Ta vs SiO_2 (c), MgO (d) and TiO_2 (e) for global arc magmas ($n = 9116$, from http://georoc.mpch-mainz.gwdg.de/georoc/) with the average Nb/Ta ratios (red points) shown to indicate the bulk Nb/Ta fractionation trend. [Data were filtered to exclude cumulates and samples with ignition loss higher than 5·0 wt %. For consistency and accuracy, the data were further filtered to include only (1) Nb and Ta determined by ICP-MS and (2) Ta contents higher than 0·05 ppm.] These diagrams show that the Nb/Ta ratio of arc magmas generally decreases with increasing SiO_2 and decreasing MgO and TiO_2, indicating a gradual decrease in Nb/Ta ratio during arc magma evolution. The global or average trend is controlled by removal of amphibole (± biotite) rather than Ti-rich phases, because the latter have a Nb/Ta fractionation trend opposite to the global trend and the amphibole-effect trend (f). (See text for details.)

amphibole fractionation results in not only a Nb/Ta decrease, but also an enhancement of the negative Ti anomaly in evolved magmas.

Amphibole fractionation and continental crust formation

The bulk continental crust is andesitic and andesite is typically formed at subduction zones (Rudnick & Fountain, 1995). The bulk continental crust has a Nb/Ta ratio of 12–13 (Barth *et al.*, 2000), whereas the parent arc basalts have an average Nb/Ta of ~15 (Munker *et al.*, 2004). This means that creating the former from the latter requires a lowering of Nb/Ta by at least 2–3 units. An estimation of the amount of amphibole required to be removed for this reduction in Nb/Ta is thus of importance for understanding the role of amphibole fractionation in continental crust formation. A recent study (Lee & Bachmann, 2014) has demonstrated that, although magma mixing is common, fractional crystallization is the dominant process generating intermediate–felsic magmas in arc settings. Crystal–liquid fractionation

in magmatic systems is believed to be controlled by the degree of crystallization. The optimum crystal fraction for melt extraction from a crystalline mush is 50–70% (Dufek & Bachmann, 2010) and for typical arc magmas it is ~60% (Lee & Bachmann, 2014). Therefore, an equilibrium crystallization model with a crystal fraction of 60% and variable amphibole in the crystal assemblage was used to calculate the variation of Nb/Ta in the melt. We used amphibole/melt $D_{Nb}/D_{Ta} = 1{\cdot}20$, 1·27, 1·40 and 1·60 for the calculations and use the average $D_{Nb} = 0{\cdot}53$ and $D_{Nb}/D_{Ta} = 1{\cdot}27$ (Table 6) at 1·0 GPa, 900–950°C and an initial H_2O of 3·0–4·3 wt % (close to 3·9 wt %) to approximately represent the amphibole/melt Nb and Ta partition coefficients during continental crust formation. Modeling results (Fig. 15a) show the following: (1) lowering the Nb/Ta in melt by 2–3 units requires amphibole/melt $D_{Nb}/D_{Ta} > 1{\cdot}20$ and >90 wt % amphibole in the residual assemblage; (2) with the average $D_{Nb}/D_{Ta} = 1{\cdot}27$, lowering by 2–3 units of Nb/Ta in the melt from 15 (parent basalt) to 12–13 (bulk continental crust) requires > 50 wt % amphibole in the crystal assemblage. The results thus suggest that generating the bulk continental crust requires amphibole as a main fractionation phase. It should be noted that this is just a very simple model and how accurate it is depends on many factors such as the roles of biotite and Ti-rich phases in the crystal assemblage and the representativeness of the Nb abundance and Nb/Ta in the parent arc magmas.

Amphibole fractionation in arc crustal roots has been widely considered as an important process for producing intermediate–felsic magmas (e.g. Dessimoz *et al.*, 2012; Solano *et al.*, 2012). Several lines of evidence include the following.

1. Experimental petrology [this study (Fig. 4); Muntener & Ulmer, 2006; Ulmer, 2007; Krawczynski *et al.*, 2012] has demonstrated that amphibole is the dominant crystalline phase in hydrous basaltic systems under the *P–T* conditions of the middle to lower crust (0·5–1·5 GPa and <1000°C). This study shows that amphibole in all except for two runs is the main crystalline phase in the crystalline assemblages (Table 3), and in the initial H_2O range close to the arc magma average of 3·9 wt %, the degrees of crystallinity are 50–70 wt %, of which amphibole accounts for >50 wt % (Table 6).
2. The change in the Dy/Yb ratios with differentiation in many arc suites can be explained only by removal of amphibole, as demonstrated by Davidson *et al.* (2007).
3. Observations on several exposed lower crustal sections (Larocque & Canil, 2010; Dessimoz *et al.*, 2012; Jagoutz & Schmidt, 2012) demonstrate that amphibole is the main fractionationing phase in arc magmas.

Although this study and many previous studies suggest that amphibole plays a key role in arc magma evolution, amphibole is not present, or its phenocrysts are rare in many arc volcanic rocks. This seems to imply that the role of amphibole is not very important in arc magma evolution. However, amphibole produced in the deep crust will be dissolved and finally disappear during magma uprise owing to its temperature stability at low pressures (<0·5 GPa) being lower than in crustal roots (1·0–1·5 GPa) (Fig. 4). This explains the paucity of amphibole in arc volcanic rocks. Smith (2014) demonstrated that clinopyroxene is the precursor to amphibole in the erupted rocks in Savo, Solomon Islands, providing evidence that amphibole can fractionate cryptically in lower crustal 'hot zones'.

The fate of amphibole-rich cumulates at the base of arc crust

A consequence of the amphibole-dominated fractionation of arc magmas is the formation of large volumes

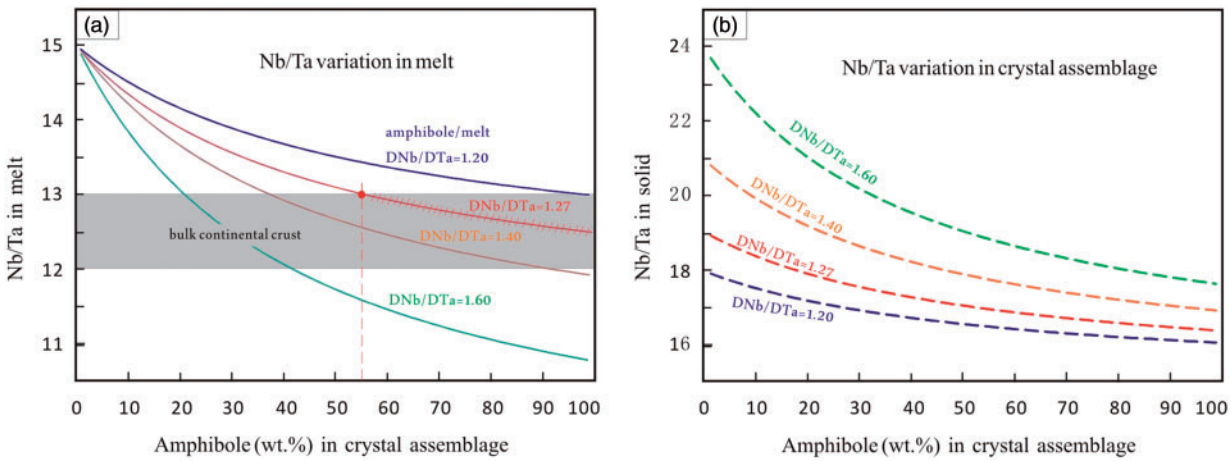

Fig. 15. Nb/Ta in melt (a) and in solid (b) vs amphibole (wt %) in the crystal assemblage for equilibrium crystallization calculations using a parent basalt with Nb/Ta = 15 and amphibole/melt $D_{Nb}/D_{Ta} = 1{\cdot}20$, 1·27, 1·40 and 1·60. The results show that lowering by 2–3 units of Nb/Ta in the melt (from 15 in the parent basalt to 12–13 in the bulk continental crust) requires amphibole as a main phase in the crystal assemblage. (The calculation adopted a 60 wt % crystal fraction for typical melt segregation and assumed that amphibole is the only phase causing the Nb/Ta fractionation; see text for details.)

of mafic cumulates with high Nb/Ta ratios in arc crustal roots, as demonstrated by the experimental results in Table 3 and the calculated results in Fig. 15b. Later tectonic thickening and metamorphism and/or partial melting may lead to transformation of such cumulates to denser eclogites, leading to delamination and the foundering of the metamorphosed cumulates back into the mantle (e.g. Lee & Bachmann, 2014; Tiepolo & Vannucci, 2014). Such a model explains not only how andesitic continental crust could form but also the possible Nb/Ta imbalance of the Earth's silicate reservoirs.

The Nb/Ta ratios of the continental crust and other reservoirs in the accessible silicate Earth are sub-chondritic, which has been explained as being due to Nb storage in the core (e.g. Munker *et al.*, 2003), or to the presence of hidden reservoirs with super-chondritic Nb/Ta in the deep mantle (e.g. Rudnick *et al.*, 2000), unless the Earth's Nb/Ta itself is sub-chondritic (Campbell & O'Neill, 2012). In the context of chondritic Nb/Ta, potential super-chondritic Nb/Ta reservoirs in the silicate Earth have been suggested to be lower crustal biotite-rich granulites (Stepanov & Hermann, 2013) and amphibole-rich mafic cumulates (Tiepolo & Vannucci, 2014), subcontinental lithospheric mantle (Pfander *et al.*, 2012), or eclogites hidden in the deep mantle (Rudnick *et al.*, 2000) or in the 'D' layer at the core–mantle boundary owing to the subduction of the Hadean crust with high Nb/Ta ratios (Nebel *et al.*, 2010). There is growing evidence that amphibole-rich cumulates formed at the base of arc crust have high Nb/Ta ratios. Nb/Ta ratios in amphibole-rich mafic and ultramafic rocks from orogenic settings worldwide generally scatter above the chondritic value [see the compilation of Tiepolo & Vannucci (2014)]. Tiepolo & Vannucci (2014) modeled the Nb and Ta contents of the hidden reservoir using mass-balance calculations. The result shows that amphibole-rich lower crust can solve the Nb/Ta imbalance if large volumes of such cumulates have been transformed to denser eclogites, which then delaminated into the mantle during the Earth's history. Although this is only a calculated result, eclogite xenoliths from the mantle (Rudnick *et al.*, 2000) and some high Nb/Ta continental basalts and ocean island basalts (OIB) that originated from the partial melting of eclogite + peridotite (Munker *et al.*, 2003; Pfander *et al.*, 2012) all suggest that most of the metamorphosed cumulates may have been returned to the mantle.

Nb/Ta fractionation and Archean TTG genesis

Archean TTG granitoids compose most of the Earth's early continental crust. Although the tectonic environment is still unclear, TTG magmas are generally believed to be generated by partial melting of metamorphosed basalts as a result of the high geothermal gradient during the Archean (e.g. Drummond & Defant, 1990; Condie, 2005). These Na-rich granitoids also have pronounced negative Nb–Ta and Ti anomalies and are characterized by high Sr/Y and strong depletion in heavy rare earth elements. The latter suggests that TTG magmas formed via partial melting of garnet-bearing protoliths (i.e. eclogite or garnet amphibolite). However, TTG genesis has been debated for a long time owing to poor understanding of the Nb/Ta fractionation during their formation.

TTG rocks have generally been thought, owing to the lack of high-precision Nb/Ta data, to have a low average Nb/Ta ratio similar to that of the present-day bulk continental crust. This led some researchers such as Foley *et al.* (2002) to propose that TTG magmas were formed by the partial melting of garnet amphibolite. However, Rapp *et al.* (2003) pointed out that the pronounced negative Nb–Ta anomaly in TTG magmas is difficult to explain by residual amphibole, because of its relatively weak ability to cause a negative Nb–Ta anomaly. Their experiments (using a low Nb/Ta protolith) demonstrated that TTG magmas can be produced by the partial melting of eclogite and that the low Nb/Ta signature is, in general, the result of inheritance. Subsequent experiments by Adam *et al.* (2012) also demonstrated that the characteristics of most incompatible elements (including the negative Nb anomaly) in TTG melts is an inheritance from their parent rocks.

Over the last 15 years, high-precision Nb and Ta data have been accumulated with the development of analytical techniques. The Nb/Ta ratios of TTG rocks turn out to be highly variable, as determined for TTG rocks worldwide by Hoffmann *et al.* (2011) using the ICP-MS technique. Compiled high-precision Nb and Ta data determined with ICP-MS for global Archean TTG rocks (Xiong *et al.*, 2011) indicate that TTG have a Nb/Ta range from 5 to >30, with an average of 14·5 ($n = 458$). Jochum *et al.* (2001) determined Nb/Ta ratios of komatiitic basalts from six Archean greenstone belts and obtained an Nb/Ta average of 14. This indicates that the Archean mantle and basalts derived therefrom should also have a similar average Nb/Ta because the large melting degree required for the generation of komatiitic basalts cannot change the Nb/Ta ratio. Given the high variability of Nb/Ta ratios in Archean TTG rocks, their formation could be explained by partial melting of both eclogite and garnet amphibolite, depending on the thermal regime. The high Nb/Ta ratios of the TTG can be explained by the melting of rutile-bearing eclogite (as a result of rutile elevating the Nb/Ta ratio in the coexisting melt), whereas their low Nb/Ta end-members could also easily be explained by the melting of garnet amphibolite. The intermediate Nb/Ta ratios would be inherited from their parent basalts, and can be explained by both eclogite melting and garnet amphibolite melting.

CONCLUSIONS

1. This study found that temperature and melt H_2O content, in addition to amphibole Mg# and melt polymerization, are the main factors affecting amphibole/melt Nb, Ta and Ti partitioning in

hydrous basaltic systems. D_{Nb}, D_{Ta}, D_{Ti} and D_{Nb}/D_{Ta} decrease with increasing temperature, melt H_2O content and amphibole Mg#, but increase with increasing melt polymerization.

2. During cooling-induced crystallization of arc magmas in crustal roots, Nb/Ta fractionation by amphibole critically depends on temperature and melt H_2O content. At a given melt H_2O content, D_{Nb}, D_{Ta}, D_{Ti} and D_{Nb}/D_{Ta} will increase and Nb/Ta fractionation will thus be enhanced with crystallization progress as a result of cooling crystallization leading to a decrease in amphibole Mg# and an increase in melt polymerization.
3. Only low temperatures, or low H_2O contents at high temperatures, lead to high amphibole/melt D values. At the arc magma average H_2O of $\sim$3·9 wt %, D_{Nb} and D_{Nb}/D_{Ta} are in general $>$0·40 and $>$1·20, respectively, which explains why amphibole fractionation results in lower Nb/Ta ratios in the evolved arc magmas. The bulk Nb/Ta fractionation trend during arc magma evolution appears to be generally controlled by amphibole fractionation, and the experimental and modeling results suggest that amphibole is a main fractionation phase during arc magma evolution and continental crust formation.

ACKNOWLEDGEMENTS

We thank P. J. Lin, Z. Q. Li and L. L. Chen for help with the electron microprobe analyses, and C. Y. Li, C. C. Zhang, L. P. Zhang and K. Wu for help with the LA-ICP-MS analyses. Constructive comments from three reviewers Massimo Tiepolo, John Adam and an anonymous reviewer and the editor Jörg Hermann have helped to substantially improve the paper. The authors gratefully acknowledge Professor Jörg Hermann and Dr Bin Fu for the correction of the English. This is Contribution No. IS-2322 from GIGCAS.

FUNDING

Financial support is acknowledged from the Strategic Priority Research Program (B) of the Chinese Academy of Sciences (XDB1820103, QYZDJ-SSW-DQC012 and GIG135PY201601), the NSF and NBRP of China (41373061, 41121002, 41173070 and 2014CB440802). This is contribution No.IS-2322 from GIGCAS.

SUPPLEMENTARY DATA

Supplementary data for this paper are available at *Journal of Petrology* online.

REFERENCES

Adam, J. & Green, T. (2003). The influence of pressure, mineral composition and water on trace element partitioning between clinopyroxene, amphibole and basanitic melts. *European Journal of Mineralogy* **15**, 831–841.

Adam, J. & Green, T. (2006). Trace element partitioning between mica- and amphibole-bearing garnet lherzolite and hydrous basanitic melt: 1. Experimental results and the investigation of controls on partitioning behaviour. *Contributions to Mineralogy and Petrology* **152**, 1–17.

Adam, J., Green, T. H. & Sie, S. H. (1993). Proton microprobe determined partitioning of Rb, Sr, Ba, Y, Zr, Nb and Ta between experimentally produced amphiboles and silicate melts with variable F content. *Chemical Geology* **109**, 29–49.

Adam, J., Green, T. H., Sie, S. H. & Ryan, C. G. (1997). Trace element partitioning between aqueous fluids, silicate melts and minerals. *European Journal of Mineralogy* **9**, 569–584.

Adam, J., Oberti, R., Camara, F. & Green, T. H. (2007). An electron microprobe, LAM-ICP-MS and single-crystal X-ray structure refinement study of the effects of pressure, melt-H_2O concentration and fO_2 on experimentally produced basaltic amphiboles. *European Journal of Mineralogy* **19**, 641–655.

Adam, J., Rushmer, T., O'Neil, J. & Francis, D. (2012). Hadean greenstones from the Nuvvuagittuq fold belt and the origin of the Earth's early continental crust. *Geology* **40**, 363–366.

Adam, J., Locmelis, M., Afonso, J. C., Rushmer, T. & Fiorentini, M. L. (2014). The capacity of hydrous fluids to transport and fractionate incompatible elements and metals within the Earth's mantle. *Geochemistry, Geophysics, Geosystems* **15**, 2241–2253.

Ballhaus, C., Berry, R. F. & Green, D. H. (1991). High-pressure experimental calibration of the olivine–orthopyroxene–spinel oxygen geobarometer—implications for the oxidation-state of the upper mantle. *Contributions to Mineralogy and Petrology* **107**, 27–40.

Barth, M. G., McDonough, W. F. & Rudnick, R. L. (2000). Tracking the budget of Nb and Ta in the continental crust. *Chemical Geology* **165**, 197–213.

Brenan, J. M., Shaw, H. F., Ryerson, F. J. & Phinney, D. L. (1995). Experimental determination of trace-element partitioning between pargasite and a synthetic hydrous andesitic melt. *Earth and Planetary Science Letters* **135**, 1–11.

Burnham, A. D., Berry, A. J., Wood, B. J. & Cibin, G. (2012). The oxidation states of niobium and tantalum in mantle melts. *Chemical Geology* **330**, 228–232.

Campbell, I. H. & O'Neill, H. S. C. (2012). Evidence against a chondritic Earth. *Nature* **483**, 553–558.

Cartier, C., Hammouda, T., Boyet, M., Bouhifd, M. A. & Devidal, J. L. (2014). Redox control of the fractionation of niobium and tantalum during planetary accretion and core formation. *Nature Geoscience* **7**, 573–576.

Caulfield, J. T., Turner, S. P., Dosseto, A., Pearson, N. J. & Beier, C. (2008). Source depletion and extent of melting in the Tongan sub-arc mantle. *Earth and Planetary Science Letters* **273**, 279–288.

Condie, K. C. (2005). TTGs and adakites: Are they both slab melts? *Lithos* **80**, 33–44.

Dalpé, C. & Baker, D. R. (2000). Experimental investigation of large-ion-lithophile-element-, high-field-strength-element- and rare-earth-element-partitioning between calcic amphibole and basaltic melt: The effects of pressure and oxygen fugacity. *Contributions to Mineralogy and Petrology* **140**, 233–250.

Danyushevsky, L. V. & Sobolev, A. V. (1996). Ferric–ferrous ratio and oxygen fugacity calculations for primitive mantle-derived melts: Calibration of an empirical technique. *Mineralogy and Petrology* **57**, 229–241.

Davidson, J., Turner, S., Handley, H., Macpherson, C. & Dosseto, A. (2007). Amphibole 'sponge' in arc crust? *Geology* **35**, 787–790.

Dessimoz, M., Muntener, O. & Ulmer, P. (2012). A case for hornblende dominated fractionation of arc magmas: The Chelan complex (Washington Cascades). *Contributions to Mineralogy and Petrology* **163**, 567–589.

Devine, J. D., Gardner, J. E., Brack, H. P., Layne, G. D. & Rutherford, M. J. (1995). Comparison of microanalytical methods for estimating H_2O contents of silicic volcanic glasses. *American Mineralogist* **80**, 319–328.

Drummond, M. S. & Defant, M. J. (1990). A model for trondhjemite–tonalite–dacite genesis and crustal growth via slab melting—Archean to modern comparisons. *Journal of Geophysical Research: Solid Earth and Planets* **95**, 21503–21521.

Dufek, J. & Bachmann, O. (2010). Quantum magmatism: Magmatic compositional gaps generated by melt–crystal dynamics. *Geology* **38**, 687–690.

Falloon, T. J. & Danyushevsky, L. V. (2000). Melting of refractory mantle at 1·5, 2 and 2·5 GPa under, anhydrous and H_2O-undersaturated conditions: Implications for the petrogenesis of high-Ca boninites and the influence of subduction components on mantle melting. *Journal of Petrology* **41**, 257–283.

Foley, S., Tiepolo, M. & Vannucci, R. (2002). Growth of early continental crust controlled by melting of amphibolite in subduction zones. *Nature* **417**, 837–840.

Gaetani, G. A. & Grove, T. L. (1998). The influence of water on melting of mantle peridotite. *Contributions to Mineralogy and Petrology* **131**, 323–346.

Gagnon, J. E., Fryer, B. J., Samson, I. M., Williams-Jones, A. E. (2008). Quantitative analysis of silicate certified reference materials by la-icpms with and without an internal standard. *Journal of Analytical Atomic Spectrometry* **23**, 1529–1537.

Green, T. H. & Pearson, N. J. (1986). Ti-rich accessory phase saturation in hydrous mafic–felsic compositions at high *P*,*T*. *Chemical Geology* **54**, 185–201.

Hawkesworth, C. J. & Kemp, A. I. S. (2006). Evolution of the continental crust. *Nature* **443**, 811–817.

Hilyard, M., Nielsen, R. L., Beard, J. S., Patiño-Douce, A. & Blencoe, J. (2000). Experimental determination of the partitioning behavior of rare earth and high field strength elements between pargasitic amphibole and natural silicate melts. *Geochimica et Cosmochimica Acta* **64**, 1103–1120.

Hoffmann, J. E., Munker, C., Naeraa, T., Rosing, M. T., Herwartz, D., Garbe-Schonberg, D. & Svahnberg, H. (2011). Mechanisms of Archean crust formation inferred from high-precision HFSE systematics in TTGs. *Geochimica et Cosmochimica Acta* **75**, 4157–4178.

Jagoutz, O. & Schmidt, M. W. (2012). The formation and bulk composition of modern juvenile continental crust: The Kohistan arc. *Chemical Geology* **298**, 79–96.

Jochum, K. P., Stolz, A. J. & McOrist, G. (2000). Niobium and tantalum in carbonaceous chondrites: Constraints on the solar system and primitive mantle niobium/tantalum, zirconium/niobium, and niobium/uranium ratios. *Meteoritics and Planetary Science* **35**, 229–235.

Jochum, K. P., Polat, A., Stoll, B., & Hofmann, A. W. (2001). Low Nb/Ta in the Archean Mantle: Ancient Missing Niobium in the Silicate Earth. *Trans. Am. Geophys. Union* 82 (Fall meeting, F1314). Abstracts.

John, T., Klemd, R., Klemme, S., Pfander, J. A., Hoffmann, J. E. & Gao, J. (2011). Nb–Ta fractionation by partial melting at the titanite–rutile transition. *Contributions to Mineralogy and Petrology* **161**, 35–45.

Kessel, R., Ulmer, P., Pettke, T., Schmidt, M. W. & Thompson, A. B. (2005). The water–basalt system at 4 to 6 GPa: Phase relations and second critical endpoint in a K-free eclogite at 700 to 1400°C. *Earth and Planetary Science Letters* **237**, 873–892.

Klein, M., Stosch, H. G. & Seck, H. A. (1997). Partitioning of high field-strength and rare-earth elements between amphibole and quartz-dioritic to tonalitic melts: An experimental study. *Chemical Geology* **138**, 257–271.

Krawczynski, M. J., Grove, T. L. & Behrens, H. (2012). Amphibole stability in primitive arc magmas: Effects of temperature, H_2O content, and oxygen fugacity. *Contributions to Mineralogy and Petrology* **164**, 317–339.

Kress, V. C. & Carmichael, I. S. E. (1991). The compressibility of silicate liquids containing Fe_2O_3 and the effect of composition, temperature, oxygen fugacity and pressure on their redox states. *Contributions to Mineralogy and Petrology* **108**, 82–92.

Larocque, J. & Canil, D. (2010). The role of amphibole in the evolution of arc magmas and crust: The case from the Jurassic Bonanza arc section, Vancouver Island, Canada. *Contributions to Mineralogy and Petrology* **159**, 475–492.

Leake, B. E., Woolley, A. R., Arps, C. E. S., et al. (1997). Nomenclature of amphiboles: Report of the subcommittee on amphiboles of the International Mineralogical Association, commission on new minerals and mineral names. *American Mineralogist* **82**, 1019–1037.

Lee, C. T. A. & Bachmann, O. (2014). How important is the role of crystal fractionation in making intermediate magmas? Insights from Zr and P systematics. *Earth and Planetary Science Letters* **393**, 266–274.

Linnen, R. L. & Keppler, H. (1997). Columbite solubility in granitic melts: Consequences for the enrichment and fractionation of Nb and Ta in the Earth's crust. *Contributions to Mineralogy and Petrology* **128**, 213–227.

Liu, X. C., Xiong, X. L., Audetat, A., Li, Y., Song, M. S., Li, L., Sun, W. D. & Ding, X. (2014). Partitioning of copper between olivine, orthopyroxene, clinopyroxene, spinel, garnet and silicate melts at upper mantle conditions. *Geochimica et Cosmochimica Acta* **125**, 1–22.

Liu, X. C., Xiong, X. L. & Audetat, A., Li, Y. (2015). Partitioning of Cu between mafic minerals, Fe–Ti oxides and intermediate to felsic melts. *Geochimica et Cosmochimica Acta* **151**, 86–102.

Liu, Y. S., Hu, Z. C., Gao, S., Gunther, D., Xu, J., Gao, C. G. & Chen, H. H. (2008). *In situ* analysis of major and trace elements of anhydrous minerals by LA-ICP-MS without applying an internal standard. *Chemical Geology* **257**, 34–43.

Maurel, C. & Maurel, P. (1982). Experimental investigation of aluminum partitioning between chromian spinel and silicate melt—petrogenetic implications—chromium content of spinels. *Bulletin de Minéralogie* **105**, 197–202.

Melekhova, E., Annen, C. & Blundy, J. (2013). Compositional gaps in igneous rock suites controlled by magma system heat and water content. *Nature Geoscience* **6**, 385–390.

Morgan, G. B. & London, D. (1996). Optimizing the electron microprobe analysis of hydrous alkali aluminosilicate glasses. *American Mineralogist* **81**, 1176–1185.

Munker, C., Pfander, J. A., Weyer, S., Buchl, A., Kleine, T. & Mezger, K. (2003). Evolution of planetary cores and the Earth–Moon system from Nb/Ta systematics. *Science* **301**, 84–87.

Munker, C., Worner, G., Yogodzinski, G. & Churikova, T. (2004). Behaviour of high field strength elements in subduction zones: Constraints from Kamchatka–Aleutian arc lavas. *Earth and Planetary Science Letters* **224**, 275–293.

Muntener, O. & Ulmer, P. (2006). Experimentally derived high-pressure cumulates from hydrous arc magmas and consequences for the seismic velocity structure of lower arc crust. *Geophysical Research Letters* **33**, 5.

Nebel, O., van Westrenen, W., Vroon, P. Z., Wille, M. & Raith, M. M. (2010). Deep mantle storage of the Earth's missing

niobium in late-stage residual melts from a magma ocean. *Geochimica et Cosmochimica Acta* **74**, 4392–4404.

Nielsen, R. L. (1990). Simulation of igneous differentiation processes. In: Nicholls, J. & Russell, J. K. (eds) *Modern Methods of Igneous Petrology: Understanding Magmatic Processes. Mineralogical Society of America, Reviews in Mineralogy* **24**, 65–105.

Nielsen, R. L. & Beard, J. S. (2000). Magnetite–melt HFSE partitioning. *Chemical Geology* **164**, 21–34.

Pfander, J. A., Jung, S., Munker, C., Stracke, A. & Mezger, K. (2012). A possible high Nb/Ta reservoir in the continental lithospheric mantle and consequences on the global Nb budget—evidence from continental basalts from central Germany. *Geochimica et Cosmochimica Acta* **77**, 232–251.

Pichavant, M., Mysen, B. O. & Macdonald, R. (2002). Source and H_2O content of high-MgO magmas in island arc settings: An experimental study of a primitive calc-alkaline basalt from St. Vincent, Lesser Antilles arc. *Geochimica et Cosmochimica Acta* **66**, 2193–2209.

Plank, T., Kelley, K. A., Zimmer, M. M., Hauri, E. H. & Wallace, P. J. (2013). Why do mafic arc magmas contain similar to 4 wt % water on average?. *Earth and Planetary Science Letters* **364**, 168–179.

Qian, Q. & Hermann, J. (2013). Partial melting of lower crust at 10–15 kbar: Constraints on adakite and TTG formation. *Contributions to Mineralogy and Petrology* **165**, 1195–1224.

Rapp, R. P., Shimizu, N. & Norman, M. D. (2003). Growth of early continental crust by partial melting of eclogite. *Nature* **425**, 605–609.

Robinson, P., Schumacher, J. C. & Spear, F. S. (1982). Phase relations of metamorphic amphiboles: Natural occurrence and theory. In: Veblen, D. R. & Ribbe, P. H. (eds) *Amphiboles: Petrology and Experimental Phase Relations. Mineralogical Society of America, Reviews in Mineralogy* **9B**, 88–98.

Rudnick, R. L. & Fountain, D. M. (1995). Nature and composition of the continental crust—a lower crustal perspective. *Reviews of Geophysics* **33**, 267–309.

Rudnick, R. & Gao, S. (2003). The role of lower crustal recycling in continent formation. *Geochimica et Cosmochimica Acta* **67**, A403–A403.

Rudnick, R. L., Barth, M., Horn, I. & McDonough, W. F. (2000). Rutile-bearing refractory eclogites: Missing link between continents and depleted mantle. *Science* **287**, 278–281.

Ryerson, F. J. & Watson, E. B. (1987). Rutile saturation in magmas—implications for Ti–Nb–Ta depletion in island-arc basalts. *Earth and Planetary Science Letters* **86**, 225–239.

Schmidt, M. W. & Poli, S. (1998). Experimentally based water budgets for dehydrating slabs and consequences for arc magma generation. *Earth and Planetary Science Letters* **163**, 361–379.

Sisson, T. W. & Layne, G. D. (1993). H_2O in basalt and basaltic andesite glass inclusions from 4 subduction-related volcanos. *Earth and Planetary Science Letters* **117**, 619–635.

Smith, D. J. (2014). Clinopyroxene precursors to amphibole sponge in arc crust. *Nature Communications* **5**, 6.

Solano, J. M. S., Jackson, M. D., Sparks, R. S. J., Blundy, J. D. & Annen, C. (2012). Melt segregation in deep crustal hot zones: A mechanism for chemical differentiation, crustal assimilation and the formation of evolved magmas. *Journal of Petrology* **53**, 1999–2026.

Stepanov, A. S. & Hermann, J. (2013). Fractionation of Nb and Ta by biotite and phengite: Implications for the 'missing Nb paradox'. *Geology* **41**, 303–306.

Tiepolo, M. & Vannucci, R. (2014). The contribution of amphibole from deep arc crust to the silicate Earth's Nb budget. *Lithos* **208**, 16–20.

Tiepolo, M., Vannucci, R., Oberti, R., Foley, S., Bottazzi, P. & Zanetti, A. (2000). Nb and Ta incorporation and fractionation in titanian pargasite and kaersutite: Crystal-chemical constraints and implications for natural systems. *Earth and Planetary Science Letters* **176**, 185–201.

Tiepolo, M., Oberti, R., Zanetti, A., Vannucci, R. & Foley, S. F. (2007). Trace-element partitioning between amphibole and silicate melt. In: Hawthorne, F. C., Oberti, R., Della Ventura, G. & Mottana, A. (eds) *Amphiboles: Crystal Chemistry, Occurrence, and Health Issues. Mineralogical Society of America and Geochemical Society, Reviews in Mineralogy and Geochemistry* **67**, 417–451.

Timofeev, A., Migdisov, A. A. & Williams-Jones, A. E. (2015). An experimental study of the solubility and speciation of niobium in fluoride-bearing aqueous solutions at elevated temperature. *Geochimica et Cosmochimica Acta* **158**, 103–111.

Ulmer, P. (2007). Differentiation of mantle-derived calc-alkaline magmas at mid to lower crustal levels: Experimental and petrologic constraints. *Periodico di Mineralogia* **76**, 309–325.

Woodhead, J., Eggins, S. & Gamble, J. (1993). High-field strength and transition element systematics in island-arc and back-arc basin basalts—evidence for multiphase melt extraction and a depleted mantle wedge. *Earth and Planetary Science Letters* **114**, 491–504.

Xiao, Y. L., Sun, W. D., Hoefs, J., Simon, K., Zhang, Z. M., Li, S. G. & Hofmann, A. W. (2006). Making continental crust through slab melting: Constraints from niobium–tantalum fractionation in UHP metamorphic rutile. *Geochimica et Cosmochimica Acta* **70**, 4770–4782.

Xiong, X., Adam, J., Green, T. H., Niu, H., Wu, J. & Cai, Z. (2006). Trace element characteristics of partial melts produced by melting of metabasalts at high pressures: Constraints on the formation condition of adakitic melts. *Science in China Series D, Earth Sciences* **49**, 915–925.

Xiong, X., Keppler, H., Audetat, A., Gudfinnsson, G., Sun, W., Song, M., Xiao, W. & Yuan, L. (2009). Experimental constraints on rutile saturation during partial melting of metabasalt at the amphibolite to eclogite transition, with applications to TTG genesis. *American Mineralogist* **94**, 1175–1186.

Xiong, X., Keppler, H., Audetat, A., Ni, H., Sun, W. & Li, Y. (2011). Partitioning of Nb and Ta between rutile and felsic melt and the fractionation of Nb/Ta during partial melting of hydrous metabasalt. *Geochimica et Cosmochimica Acta* **75**, 1673–1692.

Xiong, X. L., Adam, J. & Green, T. H. (2005). Rutile stability and rutile/melt HFSE partitioning during partial melting of hydrous basalt: Implications for TTG genesis. *Chemical Geology* **218**, 339–359.

Zack, T., Kronz, A., Foley, S. F. & Rivers, T. (2002). Trace element abundances in rutiles from eclogites and associated garnet mica schists. *Chemical Geology* **184**, 97–122.